STRATEGIES FOR COMPUTING THE SCALAR SELF-FORCE ON A SCHWARZSCHILD
BACKGROUND

A General Exam Paper

Submitted to the Graduate Faculty of the
Louisiana State University and
Agricultural and Mechanical College
in partial fulfillment of the
requirements for the degree of
Ph D

in

Physics

by
Steven (Susan) Dorsher
B.S., Massachusetts Institute of Technology, 2004
M.S., The Ohio State University, 2006
M.S., University of Minnesota, 2013
December, 2017

Acknowledgments

Table of Contents

List of Tables

List of Figures

Abstract

In this document, I present progress toward self-consistent evolutions for Extreme Mass Ratio inspirals of binary black hole systems, using the scalar self-force approximation with an effective source. Self-consistent evolutions are a critical step toward calculating gravitational wave templates for LISA, in order to resolve late times in the inspiral where the timescale of the orbits evolution is shorter than a period, as the small black hole approaches the plunge.

First I describe the preliminary development of a code base in C++ based on Peter Diener's Fortran scalar self-force simulation [20]. I have successfully implemented the wave equation in flat spacetime, reproduced the wave equation in Schwarzschild spacetime without a source, and reproduced circular orbits in Schwarzschild spacetime with an effective source at roundoff precision. However, the effort to implement an independent, state-of-the-art code base was abandoned in favor of working together on Peter Diener's existing simulation when the time scale for development of the C++ code proved too long.

In the second half of this document, I present preliminary results for estimates of the errors from Peter Diener's and Barry Wardell's time domain scalar self-force simulation for eccentric orbits using Niels Warburton's frequency domain initial conditions. First I perform a first order Richardson Extrapolation to obtain the self-force at infinite Discontinuous Galkerin order, F_{inf}, then sum the spherical harmonic modes to obtain the total self-force as a function of time. Preliminary best choice Discontinuous Galerkin evolution orders, 36 to 40, are estimated based on the absolute and relative differences of the radial self force for each DG order and F_{inf} over one radial oscillation. Preliminary best choice mode-fit parameters, $l_{min} = 14$ and $l_{max} = 25$, are estimated based on residuals of the l-mode fit and discontinuities attributed to roundoff error in a surface plot of the total radial self force as a function of l_{min} and l_{max}. The contributions to the error from the number of terms in the l-mode fit, the choice of end points in the l-mode fit, and the inability to calculate the Richardson extrapolation in real time are comparable and at the level of one part in 10^4. The contribution to the error from the use of constant weight factors in the fit is insignificant. These conclusions are preliminary and will need to be evaluated more thoroughly.

Chapter 1
Introduction

1.1   Gravitational Waves

On February 11, 2016, the LIGO Scientific Collaboration announced the first detection of gravitational waves from a black hole binary inspirals, occurring on September 14, 2015, with pre-merger masses of 36 $M_\odot$ and 29 $M_\odot$ and a post merger mass of 62 $M_\odot$ at a redshift of $z = 0.09$ [23]. Two subsequent detections followed, on December 26, 2015 [24] and on January 4, 2017 [25], with masses that are about the same to within an order of magnitude. This detection was well-anticipated. Russel Hulse and Joseph Taylor were awarded the Nobel Prize in 1993 for their 1974 discovery of a binary pulsar. This, and similar pulsars yielded precise timing measurements of orbital period changes that corresponded to rates expected due to gravitational wave emission [10]. Stellar mass black holes have been known observationally for some time since the discovery of the x-ray source Cygnus X-1 in the 1960's. Active galactic nuclei at the center of galaxies have been identified as supermassive black holes since the 1960's as well. Saggitarius A^*, a supermassive black hole at the center of the Milky Way, was originally identified through radio astronomy and is also observable in the X-ray [64], but its black hole nature has been confirmed most precisely through a 16 year study of the orbits of neighboring stars [15].

All known stellar mass black holes from x-ray sources are spinning [3], the LIGO gravitational wave detections suggested or were consistent with spinning black holes [23] [24] [25], and theoretical expectations are that angular moment from the black hole formation process should be deposited in the newly formed black hole, leaving it spinning, for the case of stellar mass black holes. For the case of supermassive black holes, there are multiple formation scenarios. One model suggests that they form from mergers of massive mass black holes from the deaths of Population I stars. Another model suggests that they are formed from large scale structure collapsing first along one dimension, then subsequently along the other two, followed by mergers into larger black holes. The third model suggests a mechanism involving initial black hole

seeds at scales between these two, formed from collapsing "clouds" in the galactic disk. All of these models impart some spin to the initial seed black hole, that may or may not be retained in subsequent mergers [56]. For the purposes of this document, I consider black holes without spin, using the Schwarzschild metric.

1.2 Extreme Mass Ratio Inspirals

In an extreme mass ratio inspiral (EMRI), a stellar mass black hole, or other compact object such as a white dwarf or neutron star, orbits around a supermassive black hole. It emits energy due to gravitational waves and its orbital frequency gradually increases while its orbital radius gradually decreases. Eventually it crosses the innermost stable circular orbit and, assuming it is on a roughly circular orbit, it plunges into the black hole without completing any further orbits.

The stellar mass black hole can be a factor of 10^5 to 10^6 smaller than the mass of the supermassive black hole in an EMRI. In an intermediate mass ratio inspiral (IMRI), the mass ratio is more like 10^2 to 10^4. LISA will be sensitive to EMRI's and some IMRI's. LIGO may be sensitive to some IRMI's. It is our goal to enable to the LISA community to provide gravitational wave templates to the LISA searches in time for the LISA launch in the early 2030's. Extraordinary precision is required to perform these searches, requiring an error in the period of no more $\delta P/P < 10^{-6}$ [9]. This is especially challenging given that the EMRI system must be evolved over a much longer timescale than a single period due to the dependence of the particle's current position on its entire history. The timescale that suffices to make the neglect of this effect small will be much longer than a single period for any physical system. Based on dimensional considerations, this timescale scales as M/μ, where M is the central black hole mass and μ is the mass ratio. For a mass ratio of 10^5, approximately 10^5 wave-cycles must be evolved [9].

1.3 Self force

Consider a classical model of the atom. This is more like the Bohr model than the plum pudding model, but it doesn't make any attempt at quantization. A negatively charged electron is orbiting a positively charged nucleus. That electron emits radiation and loses energy, becoming more tightly bound. The force that causes it to move inward is called the self-force, because it is

the force of the particle interacting with its own electric field [12].

The self-force also exists in general relativity. In the simplest possible picture of general relativity, a test particle experiencing no force moves on a geodesic. However, once we bring into our picture a compact object such as a neutron star or black hole– which clearly has its own local curvature– it generates a back-reaction. It is possible to obtain the self-force in general relativity from either perturbations of the metric [45] or perturbations of the particle's world-line [59]. Either way, the small parameter governing the expansion is the mass ratio of the system. Again, the self-force is due to the interaction of the small black hole with the gravitational field itself.

In this document, we consider a slightly simpler problem, that of a scalar field on a curved space-time background. In this case, the self-force is due to the interaction of the scalar field with the particle itself. The stellar mass black hole is now a scalar delta function source that evolves along an orbit through space-time. As in the other two cases, the source causes scalar waves to be emitted that travel in all spatial directions away from the source, both toward light-like infinity and into the supermassive black hole horizon. The back-reaction causes a self-force that propels the particle slightly inward with each orbit as it loses energy to these outgoing waves. Ultimately, if evolved for that long, the particle should enter the horizon of the large black hole and then, it is beyond the scope of present day physics to say what should happen to it.

1.4   The gravitational wave sky

Currently, there are four distinct windows on the gravitational wave universe planned or in progress. The Laser Interferometer Gravitational Wave Observatory, LIGO, probably deserves first listing, due to their recent success. LIGO observes gravitational waves using a ground based Michelson-Morley interferometer with two 4 kilometer long Fabry-Perot cavity arms. It detects strains as small as $10^{-23}Hz^{-1/2}$ [37]. It has thus-far had three detections of black hole binary pairs in the tens of solar mass range. These mergers have been tracked through inspiral and merger [23] [24] [25], and ringdown [30], to produce exact tests of general relativity. LIGO has even been able to set limits on non-General Relativistic behavior, such as the magnitude of the dispersion of the intergalactic medium to gravitational waves [25] and deviation of the post

Newtonian parameters from those predicted from GR [30]. The LIGO-Virgo collaboration continues searches for neutron star binary inspirals, which may have electromagnetic counterparts in the form of supernovae; pulsars, which are thought to have raised "mountains" on their surface causing a changing quadrapole moment– these will also have electromagnetic counterparts; gravitational wave bursts correlated with EM, neutrino, or particle sources such as a gamma ray burst; or the cosmic or galactic white dwarf binary stochastic background radiation. In the future, KAGRA, an observatory in Japan, and IndIGO, an observatory in India, will join the search for gravitational waves, refining the collaboration's ability to locate a source on the sky.

The cosmic microwave background (CMB) can also be used to constrain the primordial stochastic background of gravitational waves. It is a very low frequency source, with wavelengths related to the size of the observable universe ($f \sim 10^{-17} Hz$). Searches depend upon separating the polarization into two components: the B-modes, which have curl, and the E-modes, which don't. If the B-modes and the E-modes are roughly even, then tensor components of the density perturbation dominate, and gravitational waves may be present. Micro-lensing and dust are significant noise sources that must be carefully subtracted. Current searches include BICEP2, Planck, and the Keck Array.

Pulsar timing uses the extremely precise timing of pulsars, taking their spin down into account and correlating with pairs of other pulsars. In this timing, they are looking for residual signals that may be due to supermassive black hole binaries, cosmic string cusps, and the cosmic stochastic gravitational wave background. Existing pulsar timing arrays include the Parkes Pulsar Timing Array (PPTA), the European Pulsar Timing Array (EPTA), and the North American Nanohertz Observatory for Gravitational Waves (NANOGrav). They have formed a collaboration called the International Pulsar Timing Array (IPTA). The IPTA is sensitive from 10^{-9} to 5×10^{-8} Hz with strains on the order of 10^{-14} to 10^{-15} [22].

Extreme mass ratio black hole binaries are likely to be detected only by LISA. The Laser Interferometer Space Observatory (LISA) is a space-based observatory. Like LIGO, it will use interferometry to detect gravitational waves; however, it will have three arms arranged in a trian-

gle separated by 2.5 million kilometers. Each end mirror will be in free-fall on a satellite, with the satellite stabilized by micro-thrusters. LISA Pathfinder was launched in 2015 and demonstrated the optics essential to this space-based mission can operate successfully remotely. As of June of 2017, LISA is fully funded by the European Space Agency, with NASA as a lesser partner. The launch date is set in the early 2030's. In addition to EMRI's, LISA may detect IMRI's, supermassive black hole binaries, and the primordial stochastic gravitational wave background. [2], [9], [16]

1.5   Notation

In this manuscript, I use natural units where $G = c = 1$, where $G = 6.67408 \times 10^{-11} m^3 kg^{-1} s^{-2}$ is the gravitational constant and $c = 299792458 m/s$ is the speed of light. All other quantities can be written in terms of the black hole mass. For example, lengths are naturally represented in terms of the Schwarzchild radius, $2M$, but the unit is the mass, M. The unit for time is also mass because the speed of light has units of length divided by time, which is one. Other units can be derived in a similar manner. Most interestingly, the units for energy are masses because, dimensionally, $E = \sqrt{M^2 c^4 + (pc)^2}$, in special relativity.

I use Einstein summation notation for tensors, where a repeated Greek index implies a summation over that repeated index. For example, an n dimensional tensor field of rank (1,2) transforms, in general, according to the rule

$$T^{\alpha}_{\beta\gamma}(\bar{x}^1, \ldots, \bar{x}^n) = \Lambda^{\alpha}_{\delta} \Lambda^{\varepsilon}_{\beta} \Lambda^{\zeta}_{\gamma} T^{\delta}_{\varepsilon\zeta}(x^1, \ldots, x^n) \tag{1.1}$$

where Λ is the Jacobian of the coordinate transformation from x to $\bar{x}$.

Indices are raised by use of the inverse metric and lowered by use of the metric. The metric transforms contravariant one-forms, which constitute the basis, to covariant vectors, which constitute the coordinates, e.g. $u^{\beta} = g^{\alpha\beta} u_{\beta}$, where $g^{\alpha\beta}$ is the metric. However, the metric and its inverse can also be used to raise and lower indices of tensors of higher and mixed rank. The metric describes the relative distance between two coordinates on a manifold, in all n dimensions,

in an $n \times n$ matrix. Two sign conventions are allowed, depending on whether the time component is positive or negative, though the metric always has a negative determinant in four dimensions. In our sign convention, the Minkowski metric for flat space-time is given by

$$\eta^{\mu\nu} = \eta_{\mu\nu} = \begin{bmatrix} -1 & 0 & 0 & 0 \\ 0 & 1 & 0 & 0 \\ 0 & 0 & 1 & 0 \\ 0 & 0 & 0 & 1 \end{bmatrix}$$

Here the four dimensions are Cartesian, t, x, y, and z. The Schwarzschild metric for a spherically symmetric black-hole without charge or spin is given by

$$g_{\mu\nu} = \begin{bmatrix} -(1 - \frac{2M}{r}) & 0 & 0 & 0 \\ 0 & (1 - \frac{2M}{r})^{-1} & 0 & 0 \\ 0 & 0 & r^2 & 0 \\ 0 & 0 & 0 & r^2 \sin^2 \theta \end{bmatrix}$$

where $d\tau$ is the proper time, and coordinates are t (the local time), r (a radial coordinate that goes to zero at the singularity, $2M$ at the horizon, and infinity at spatial infinity), θ (the polar angle), and ϕ (the azimuthal angle). To obtain the inverse (raised) metric, simply invert the matrix representation.

Chapter 2
A simple numerical solution for a PDE using the Discontinuous Galerkin method

2.1 Reduction to coupled first order differential equations

The fundamental problem we wish to solve is to evolve the wave equation on Schwarzschild space-time with a source. However, to begin to address this problem, I implemented a one dimensional wave equation solver in C++ using the Discontinuous Galerkin method in flat space-time. The wave equation in flat space-time is given, in several different forms, by

$$\Box \psi = 0 \tag{2.1}$$

$$\frac{\partial^2 \psi}{\partial t^2} = \nabla \psi \tag{2.2}$$

$$\frac{\partial^2 \psi}{\partial t^2} = \frac{\partial^2 \psi}{\partial r^2} \tag{2.3}$$

where the final form is specialized to one dimension and $c = 1$ in natural units. To numerically integrate this, it is necessary to reduce this second order differential equation to three coupled differential first order differential equations. There is a classical solution to this problem, which we follow. We introduce variables $\rho = \frac{\partial \psi}{\partial t}$ and $\phi = \frac{\partial \psi}{\partial r}$. With these definitions, and remembering that we want time evolution equations rather than spatial evolution equations, the three coupled equations become

$$\frac{\partial \psi}{\partial t} = \rho$$
$$\frac{\partial \rho}{\partial t} = \frac{\partial \phi}{\partial r}$$
$$\frac{\partial \phi}{\partial t} = \frac{\partial \rho}{\partial r} \tag{2.4}$$

This system of equations can be rewritten

$$\frac{\partial u}{\partial t} = A\frac{\partial u}{\partial r} + Bu = RHS(u,t)$$

where u is the state vector consisting of $u = (\psi, \rho, \phi)$, and A and B are matrices. RHS stands for Right Hand Side. The C++ code has been implemented for wave equations of this generalized form, which encompasses wave equations on a Schwarzschild space-time. For flat spacetime,

$$A = \begin{bmatrix} 0 & 0 & 0 \\ 0 & 0 & 1 \\ 0 & 1 & 0 \end{bmatrix}$$

$$B = \begin{bmatrix} 0 & 1 & 0 \\ 0 & 0 & 0 \\ 0 & 0 & 0 \end{bmatrix}$$

2.2 Spatial grids

Our code solves a wave equation, which must first calculate a spatial derivative then integrate in time to solve a differential equation. For the spatial derivative part of the scheme, we make use of the Discontinuous Galerkin method to compute spatial derivatives, as a replacement for a finite difference scheme. Its has two primary benefits. One is that it naturally handles discontinuities in the evolved field, which is important to the effective source approach that we use when calculating orbits with a source in curved space-time. The second is that its accuracy scales exponentially with increasing polynomial order.

2.2.1 Finite difference schemes

The classic solution to the spatial derivative problem is the finite difference scheme. In a one dimensional finite difference scheme, space is discretized into points on a line. The spatial derivative is calculated using a stencil of points that is symmetric about the point where one wants to know the spatial derivative, and extends n points to either side of a boundary. The

spatial derivative is calculated from a weighted sum of the $2n$ or $2n+1$ points included in the stencil, where some of the weights are negative. It is possible to expand any order of derivative to any order of expansion. A first derivative, with three points in the stencil, is given by:

$$D_r^{(1)} = \frac{1}{h}(-\frac{1}{2}f_{-1} + \frac{1}{2}f_1) \qquad (2.5)$$

Here the f_{-1} and f_1 indicate the function evaluated at the grid point to either side of the 0th grid point, where the derivative is evaluated. Here h is the spacing between grid points. A second derivative in a three point stencil is given by

$$D_r^{2,(1)} = \frac{1}{h^2}(f_{-1} - 2f_0 + f_1) \qquad (2.6)$$

It is possible to extend these stencils to two and three dimensions. When considering parallelization using OpenMP, issues of synchronization must be considered. When parallelizing over many nodes, the spatial grid gets divided into blocks. At the ends of each block, the boundary cells need information from the neighboring cells to calculate the spatial derivative. It is necessary to synchronize a number of boundary cells equal to the size of the stencil in buffer zones both to the left and to the right at each time step. In our code, this is not necessary, since we have parallelized with OpenMP, which uses shared memory within one node, across several (16) cores.

2.2.2   The Discontinuous Galerkin method

The Discontinuous Galerkin method breaks space into segments called elements. Within each element, the value of the field is represented by the sum of $n+1$ interpolating polynomials of order n, where n is the order of the element. There are $n+1$ unevenly spaced nodes in the element, clustered toward the edges. At each node, exactly one of the interpolating polynomials takes on a value of one while the others are zero. An interpolating Lagrange polynomial has a

functional form:

$$l_i(r) = \prod_{j=0, j\neq i}^{n} \frac{r - \xi_j}{\xi_i - \xi_j} \tag{2.7}$$

where ξ_i is a location of a node and where r is an arbitrary position [21].

Omitting the details of the derivation of this method, which can be found in Reference [21], the procedure for calculating the spatial derivative in one dimension is to first calculate the Legendre polynomials. A matrix inversion is involved to calculate the derivative matrices, for which we use custom packages, the Template Numerical Toolkit and JAMA. It was discovered, upon parallelization with OpenMP, that TNT is not thread-safe. I rewrote most, but not all, of the code to avoid this issue; however, it would be better to replace TNT altogether if this code were developed further.

The Discontinuous Galerkin method helps damp error introduced by discontinuities in the field, provided they remain at element boundaries. We make use of this in our self-force calculations in the neighborhood of the particle, to be described in Chapter 5.4. The numerical flux describes how information passes from one element to the next in the Discontinuous Galerkin method and is a way of accounting for the discontinuity in the flow between neighboring elements. The specific method we use for calculating the numerical flux breaks the wave velocities into in-going and outgoing components. At each element boundary, the in-going component of the flux is calculated from the far side of the element boundary and the out-going component of the flux is calculated from the inside of the element boundary. The numerical flux at that boundary is the difference. The contribution from each boundary is distributed across the element according to a lift matrix. This is repeated at each time step. Discontinuities can exist at the boundaries, but not within an element.

2.3 Time evolution

Time evolution in our code is handled by a fourth order low storage Runga Kutta method. Instead of the standard fourth order Runga Kutta method, this method takes five sub-time-steps, but only the most recent sub-time-step needs to be stored.

$$p^{(0)} = u^n$$

$$k^{(0)} = 0$$

$$k^{(i)} = a_i k^{(i-1)} + \delta t\, RHS(p^{(i-1)}, t^n + c_i \delta t)$$

$$p^{(i)} = p^{(i-1)} + b_i k^{(i)}$$

$$u_h^{n+1} = p^{(5)} \tag{2.8}$$

Here steps two and three are repeated for $i = 1 - 5$, first k, then p, then increase i and repeat. The coefficients a_i, b_i, and c_i are given in Reference [21].

2.4 Wave equation on flat space-time

Using Gaussian initial conditions in ψ and setting the ϕ (Equation 2.4) initial conditions to the derivative of that Gaussian ($\rho = 0$), I have produced the evolution shown in Figure 2.1. The Gaussian splits into two, evolves both left and right, hits the periodic boundary conditions, and re-enters the one-dimensional space on the opposite side, eventually returning to its original position and re-merging. A progression from left to right can be seen in Figure 2.2 for sinusoidal initial conditions with a sinusoidal initial condition in ψ and where I have set the initial conditions of ϕ equal to the radial derivative of ψ and ρ equal to the time derivative of ϕ (Equation 2.4). The wave moves to the right because the angular frequency is taken to be positive. Again, periodic boundary conditions cause the wave to cross to the opposite side and re-enter.

The Discontinuous Galerkin method has truncation error that scales as h^{n+1}, where h is the element size and n is the polynomial order of the elements. The L_2 error is defined as the square root of the sum of the squared differences across all space, after one complete cycle of the system. Because of the periodic boundary conditions, the system should be the same after one complete cycle, making a meaningful error estimate possible. The scaling of the L_2 error with DG order and with element size is shown in Figures 2.3 and 2.4. The scaling of Figure 2.3 matches expectations until roundoff error is hit, where the error stops improving with order or smaller element size. Not
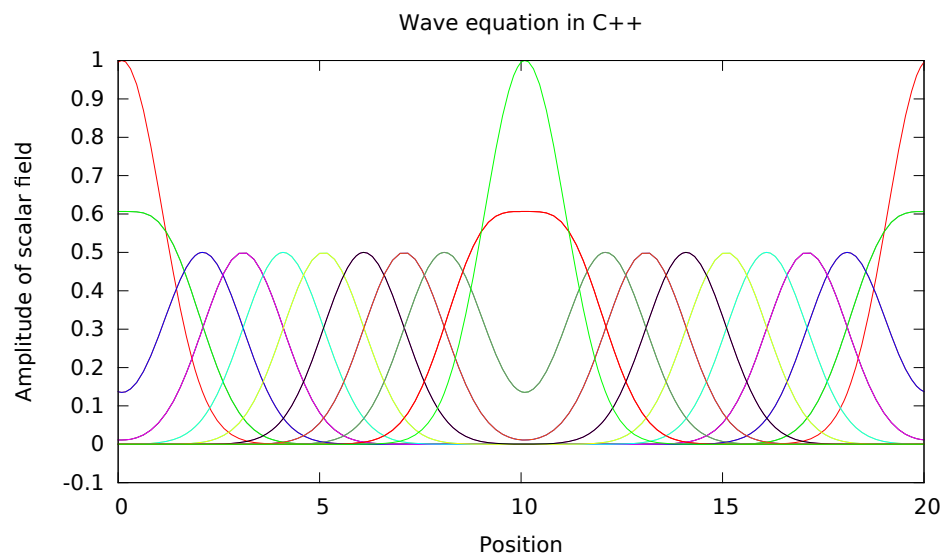
Figure 2.1: Waves evolving over time for Gaussian initial conditions
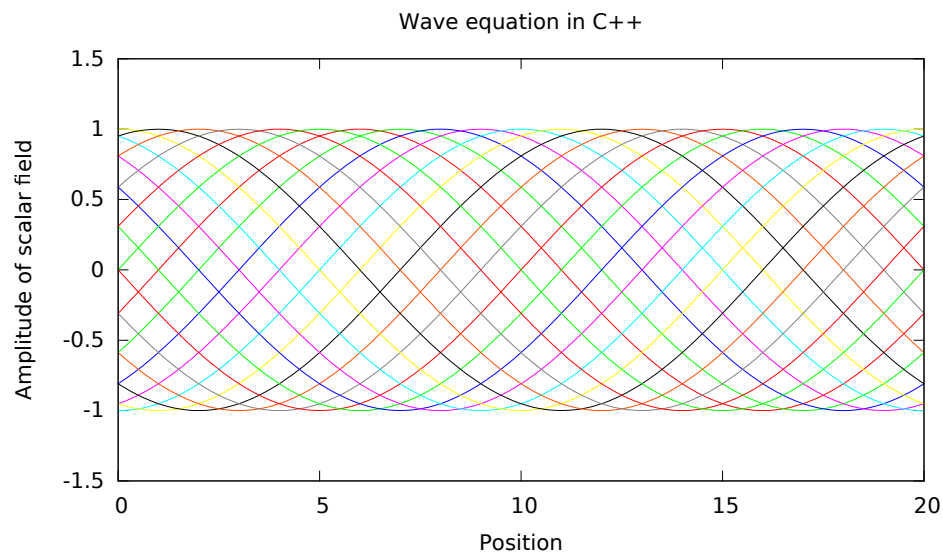
Figure 2.2: Waves evolving over time for sinusoidal initial conditions
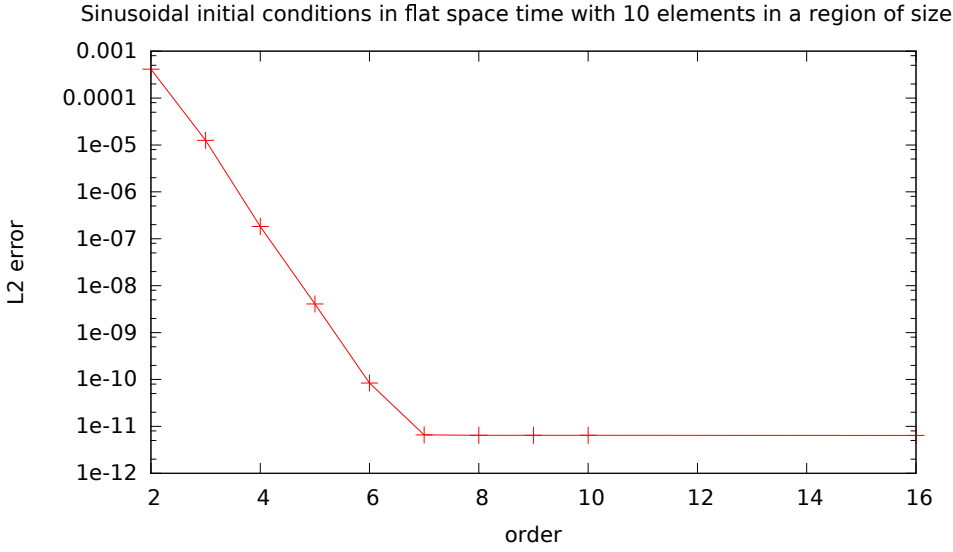
Figure 2.3: L_2 error scaling with DG order for sinusoidal initial conditions with ten elements with element size $h = 0.01$.

shown, this same pattern was seen for the L_0 error, which is the maximum error over all space. In Figure 2.4, we see super-convergent behavior where the order three simulation converges as h^5, roughly, rather than h^4. In a rather preliminary search I have not found this specific issue, of a simple one dimensional wave equation with a characteristic flux, addressed in a publication. However, super-convergent behavior in the Discontinuous Galerkin method does exist, and it is possible that this is an example generated by underlying symmetries of the wave velocities and spatial dimensions in the problem.
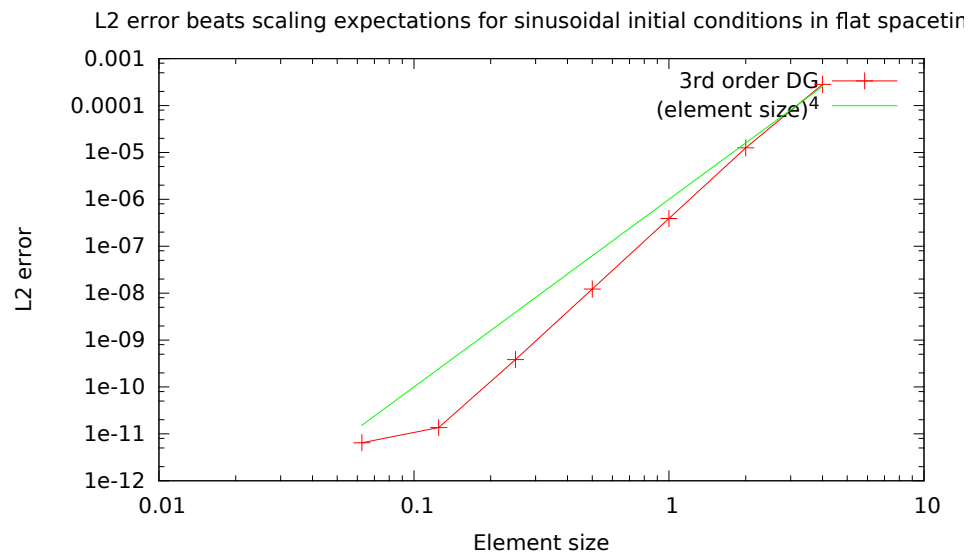
Figure 2.4: L_2 error scaling with element size for sinusoidal initial conditions. The error seems to be super-convergent. This requires cancellations due to symmetry, perhaps due to the symmetry of wave propagation speed in either direction in flat spacetime.

Chapter 3
A scalar field on a Schwarzschild background without a source

3.1 Scalar field on Schwarzschild space-time

Although the final goal in this field is to compute tensor waveforms that can be used as templates for LISA searches, for the purposes of obtaining the desired accuracy, it is important to improve our computational methods. We do this by developing numerical techniques using scalar, rather than tensor, self force methods to make the problem more tractable. In this chapter, I discuss the physical behavior of a scalar field without a source on a Schwarzschild background.

I have reimplemented Peter Diener's Fortran scalar self-force code, with a slightly modified design, in C++. The desired goal was for the results to match to within roundoff error. This was achieved for scalar fields without a source and for scalar fields with point sources on circular orbits (see Chapter 4.3). The original goal was to implement an independent state-of-the-art code base that I could parallelize in HPX, a tool which makes it simple to do high performance computing. I have implemented the original code sample given to me and parallelized that in OpenMP; however, the larger task was put on hold indefinitely in favor of working with Peter Diener on his simulation so that I could more immediately contribute to current developments in the field.

3.1.1 Scalar field wave equations

A scalar field is a field that has one one degree of freedom at a given point in space– rather than being a matrix, it has a single value. The scalar wave equation can be written, in the absence of a source, in short form, as the D'Alembertian or box operator acting on a scalar field.

$$\Box\Psi = 0 \tag{3.1}$$

In flat spacetime this reduces to the standard wave equation. In curved spacetime, further complications are introduced, to account for the curvature of space. This enters through the metric. For a scalar field, the D'Alembertian can be written

$$\Box\Psi = \frac{1}{\sqrt{-g}}\partial_\mu(\sqrt{-g}g^{\mu\nu}\partial_\nu\Psi) = 0 \tag{3.2}$$

where g is the determinant of $g_{\mu\nu}$. [57]

- **Multipole moment decomposition**

  In our approach, spherical harmonics are used to reduce the three spatial dimensions to a one dimensional problem, in terms of the radius and a sum of an infinite number of discrete spherical harmonic modes, characterized by numbers l and m, where l ranges from 0 to ∞ and m ranges from $-l$ to $+l$ for each l [43]. The field is written as

$$\Psi = \sum_{l,m}\Psi^{lm}(t,r)Y^{lm}(\theta,\phi) \tag{3.3}$$

This separation of variables ansatz can be used to simplify the wave equation in any coordinate system, since the angular coordinates are not transformed in any of the coordinate systems we use. We make use of the identity

$$r^2\nabla^2_{\theta,\phi}Y^{lm} = -l(l+1)Y^{lm} \tag{3.4}$$

where $\nabla^2_{\theta,\phi}$ is the angular part of the Laplacian, which has a $\frac{1}{r^2}$ dependence. This introduces a term proportional to $l(l+1)\Psi^{lm}(t,r)$ for each l, m.

- **Tortoise coordinates**

  In this code, we use a mixture of tortoise (Eddington-Finkelstein) and hyperboloidal coordinates. Tortoise coordinates have the property that they go to infinity at the horizon and spatial infinity. It is beneficial to place the horizon at an unreachable distance in coordinate space so that the boundary conditions at the horizon become trivial and there is no leakage of information

from the interior of the black hole to outside the horizon in the process of discretization. It is also beneficial to increase the number of computational elements near the horizon by compactifying the coordinates there. Tortoise coordinates are obtained by the following transformation of Schwarzschild coordinates. [57]

$$t_* = t \tag{3.5}$$

$$r_* = r + 2M \ln \left| \frac{r}{2M} - 1 \right| \tag{3.6}$$

$$\theta_* = \theta \tag{3.7}$$

$$\phi_* = \phi \tag{3.8}$$

We solve the wave equation in tortoise coordinates in one region of the code. I have re-derived this equation in Mathematica and verified the form that appears in Peter Diener's Fortran scalar self-force code. The wave equation in tortoise coordinates is

$$\frac{\partial^2 \psi}{\partial t^2} = \frac{\partial^2 \psi}{\partial r_*^2} - \frac{1}{r^3} \left(\frac{2M}{r} + (l+1)l \right) \left(1 - \frac{2M}{r} \right) \psi \tag{3.9}$$

r is in Schwarzschild coordinates, r_* is in tortoise coordinates, l is the spherical harmonic l-mode (discussed below), which accounts for the angular dependence, and ψ is a function of tortoise coordinates.

- **Hyperboloidal coordinates**

Hyperboloidal coordinates are necessary because infinities are computationally unreachable. It is clear that space infinitesimally close to the horizon is important, since the curvature of space is strongest there, and it is still causally connected to the exterior region. To make the horizon reachable in a finite number of computational elements, while retaining the property that more computational elements are placed near the horizon than far away, hyperboloidal coordinates are introduced in the region closest to the horizon. In a middle region, tortoise coordinates are used. In the region furthest from the black hole, hyperboloidal coordinates are used again to place

17

light-like infinity, $\mathscr{I}^+$, at a finite coordinate.

There are a few key features of the hyperboloidal transformation [5]. The angular coordinates are not transformed. The time coordinate preserves the stationarity of the background metric, and thus the new time variable, τ, must be related to the old time variable, t_*, by an offset dependent only upon r_*, $\tau = t - h(r_*)$. For in-going waves in the inner region, $t - r_* = \tau + \rho$ and in the outgoing region, $t + r_* = \tau - \rho$ to preserve the structure of the light cone. Bernuzzi, Nagar, and Zenginoglu define $H = \frac{dh}{dr_*}$. They introduce a compactification that depends on a transition function Ω [63] that goes to one at the boundaries between the hyperboloidal region and the tortoise region and remains one throughout the tortoise region, and smoothly goes to zero at the horizon and at $\mathscr{I}^+$. The tortoise coordinate is defined to be $r_* = \frac{\rho}{\Omega(\rho)}$ in the hyperboloidal region, resulting in an expression for the height function H in terms of the hyperboloidal radius, $H(\rho) = 1 - \frac{\Omega^2}{\Omega - \rho\Omega'}$. For the purpose of computing characteristic modes, important for the numerical fluxes, we are only interested in the highest derivative terms of the wave equation, called the principal part. Their final principal part of the wave equation is [5]

$$
\begin{aligned}
\partial_{t_*}^2 - \partial_{r_*}^2 = \quad & -(1-H^2)\partial_\tau^2 \\
& +(1-H)(-2H\partial_\tau\partial_\rho + (1-H)\partial_\rho^2 - (\partial_\rho H)(\partial_\tau + \partial_\rho))
\end{aligned}
\tag{3.10}
$$

I have verified this equation in Mathematica.

3.2 Theoretical expectations

The system without a source is necessary for code development; however, it is also similar to the like the ring-down phase of an EMRI system after the small black hole plunges into the super-massive black hole. There are two analytically predicted behaviors that characterize the system that has no source. Initially, there should be quasi-normal mode ringing. Eventually that fades into a long, power law tail.
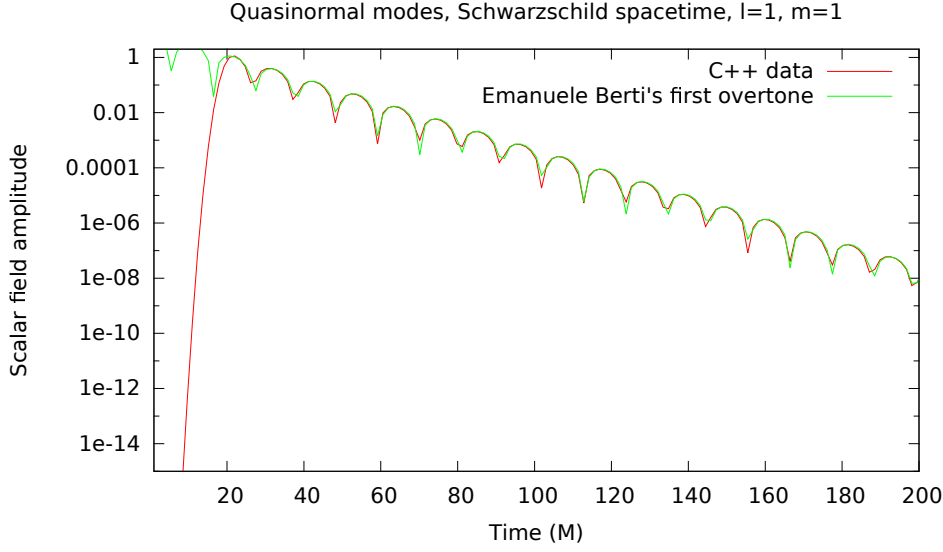
Figure 3.1: Fundamental quasi-normal mode for l=1

3.2.1 Quasi-normal modes

A field, such as a scalar or tensor field surrounding a black-hole, exhibits quasi-normal mode ringing as it relaxes into or away from the black hole. A quasi-normal mode decays at a steady frequency with an exponential decay envelope due to loss of energy from the system. These rates have been calculated by Reference [6] and made available online. I have tested their theoretical expectations for the fundamental mode at each l-mode against my simulation data in Figures 3.1 and 3.2 by plotting the QNM ringdown waveform using Berti's frequency and exponential decay parameters and adjusting the amplitudes and starting times by hand. Notice that for higher l, the quasi-normal mode frequency is higher and the decay is faster.

3.2.2 Power law tails

Quasi-normal mode ringing evolves into power law tails with a relatively rapid transition between the two regimes. Both are due to backscattering of the waves off the background metric, but QNM are due to interactions near the peak of the potential, while the power law tails are due to interactions of the field with the background spacetime far away from it. In 1972, Richard Price predicted that the tails would scale as $t^{-(2l+2)}$ or $t^{-(2l+3)}$ depending on initial conditions [48]. In our choice of initial conditions, $t^{-(2l+3)}$ is expected. Figure 3.3 shows a mode for which

19
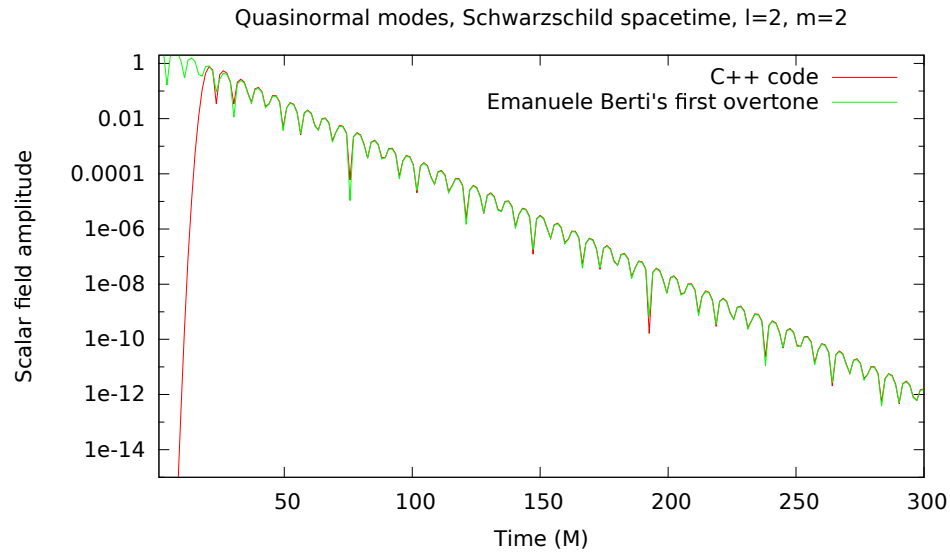
Figure 3.2: Fundamental quasi-normal mode for l=2

I successfully recovered a power law tail. Figure 3.4 demonstrates that truncation error may dominate at high l, and that it may be necessary to increase the DG order to resolve all l-modes in a simulation.
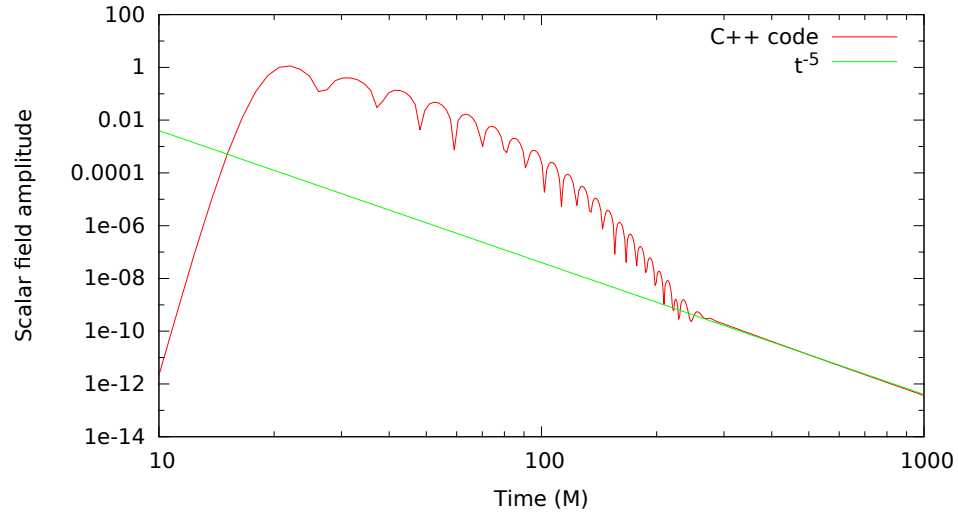
Figure 3.3: Power law tail, l=1
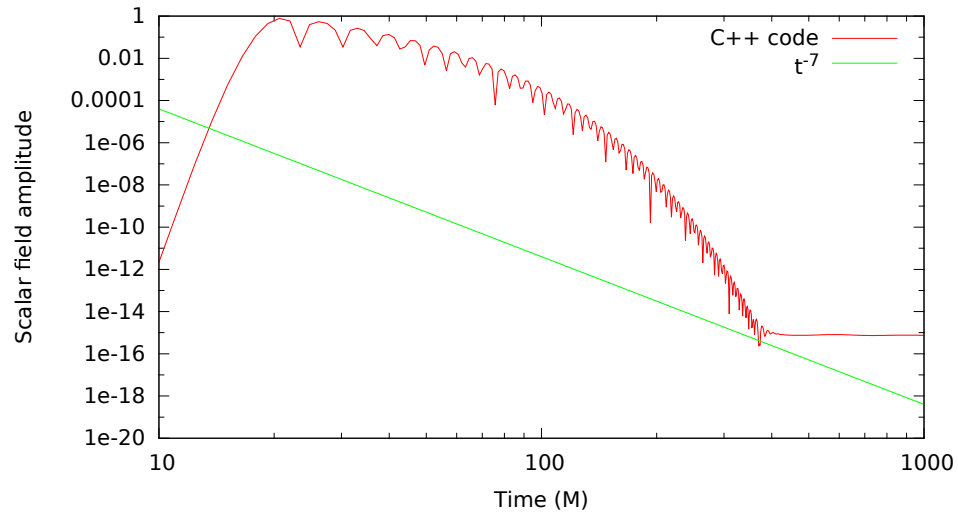
Figure 3.4: Power law tail does not match expectations due to truncation error in DG method, l=2

Chapter 4
Circular orbits on a Schwarzschild spacetime

At this point, we introduce a source to the wave equation. We consider a particle fixed on a circular orbit. A source on a circular orbit still emits radiation but requires an input of energy to the system to remain in a stationary orbit that does not inspiral. In this system, the self-force is counteracted by the force keeping the particle in its orbit. Imagine, in a science-fiction-like scenario, that the particle is a spacecraft with a compact object inside it, held in orbit by a thruster about a supermassive black hole. While this is not a physically reasonable scenario, it is a useful toy model for developing physical intuition about the effective source.

4.1 Self Force

A test particle orbiting a black hole follows a geodesic, which is the path of extremal proper time. This is described by the geodesic equation,

$$\frac{\partial^2 x^\mu}{\partial \tau^2} + \Gamma^\mu_{\rho\sigma} \frac{\partial x^\rho}{\partial \tau} \frac{\partial x^\sigma}{\partial \tau} = 0 \tag{4.1}$$

where τ is the proper time and $\Gamma^\mu_{\rho\sigma}$ is the Christoffel symbol, given by [7]

$$\Gamma^\sigma_{\mu\nu} = \frac{1}{2} g^{\sigma\rho} (\partial_\mu g_{\nu\rho} + \partial_\nu g_{\rho\mu} - \partial_\rho g_{\mu\nu}) \tag{4.2}$$

However, a black hole, of any size, is not a test particle. For an EMRI, if the full case of general relativity is considered and we do not simplify the problem to a scalar field, the additional force can be treated perturbatively in the mass ratio of the two particles. In the scalar case, the wave equation with a point particle source is simply written as a delta function source to the wave equation dependent upon the particle's position in time [59]

$$\Box \Psi^{ret} = -4\pi q \int \delta_4(x, z(\tau')) d\tau' \tag{4.3}$$

In this equation, $\square$ is the D'Alembertian and $z(\tau')$ is the evolving path of the source in space-time as a function of the particle's proper time. In the scalar approximation, the particle acts as a delta function point source, with a charge of *q* and mass *m*. That charge may accelerate or evolve with time; see chapter 8.3.

The retarded field is singular at the location of the particle due to the delta function source. Singularities are computationally problematic. To regularize this singularity, a regular field is created through the use of an effective source.The regularized field, Ψ^R, is defined in terms of the retarded field with the Detweiler-Whiting singular field, $\tilde{\Psi}^S$, subtracted.

$$\Psi^R = \Psi^{ret} - \tilde{\Psi}^S \tag{4.4}$$

The wave equation on a curve spaced time is given an effective source that depends on the location of the particle in four space.

$$\square\Psi^R = \square(\Psi^{ret} - \tilde{\Psi}^S) = S_{eff} \tag{4.5}$$

Subtraction of the Detweiler-Whiting singular field cancels the delta function. However, we only know an approximation to the Detweiler-Whiting singular field, which is is exact at the location of the particle and begins to deviate as the distance from the particle grows. This leads to the definition of an effective source, S_{eff}, which is zero outside the neighborhood of the particle due to the world tube window function, *W*, shown in Figure 4.1.

$$S_{eff} = 4\pi q \int \delta(x, z(\tau'))d\tau' - \square(W\tilde{\Psi}^S) \tag{4.6}$$

The window function is to reduce the effect at long ranges of the approximation in the Detweiler-Whiting singular field to the true singular field. Outside the range of the window function, the regularized field is equal to the retarded field.

The Detweiler-Whiting singular field is derived from convolutions of retarded and advanced
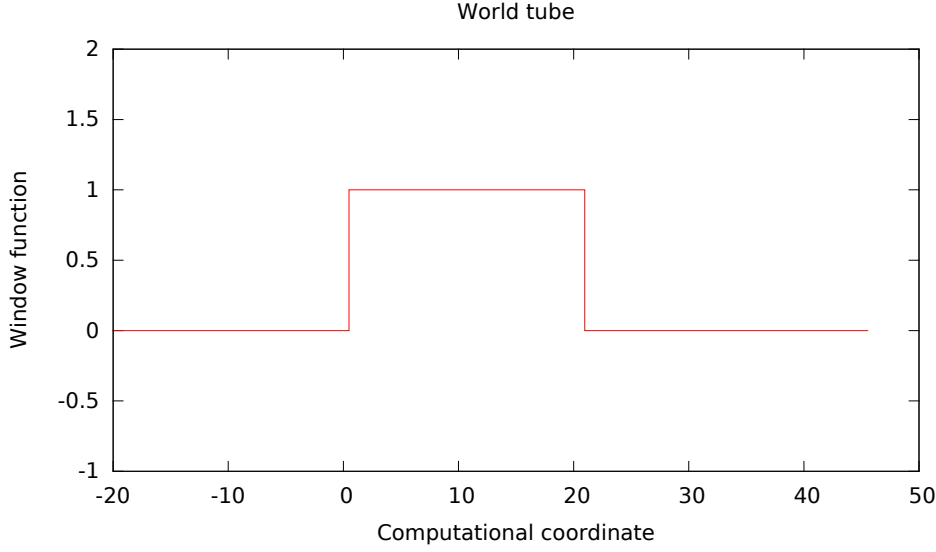
Figure 4.1: Spatial slice of the world tube window function.

Greens functions appropriately symmetrized to select the singular part [8]. It is perturbatively expanded in powers of the proper time along the particle's worldline [20] (Equation 3.7). The simulation currently incorporates the perturbative expansion to first order [20], though a second order expansion to the Detweiler-Whiting singular field based upon a different approach is currently under development [45]. The self-force in a simulation can be computed is merely a gradient of Ψ^R at the location of the particle [53].

4.2 World tube

The world tube window function around the particle carves out a spherical shell around the black hole, due to the use of spherical harmonics to compute the angular spatial dimensions in a 1+1 dimensional simulation. In my C++ code, the world tube extends throughout the entire tortoise region, ending at the transitions to the hyperboloidal regions. When calculating numerical fluxes at this boundary, it is necessary to account for both the coordinate transformations between either side of the boundary and the transformation between regular and retarded field.

4.3 Comparison between C++ and Fortran codes

I've performed a comparison between Peter Diener's Fortran code [20] and my C++ code, in both of which I ran the simulation for a scalar particle on a circular orbit of radius 10 M.
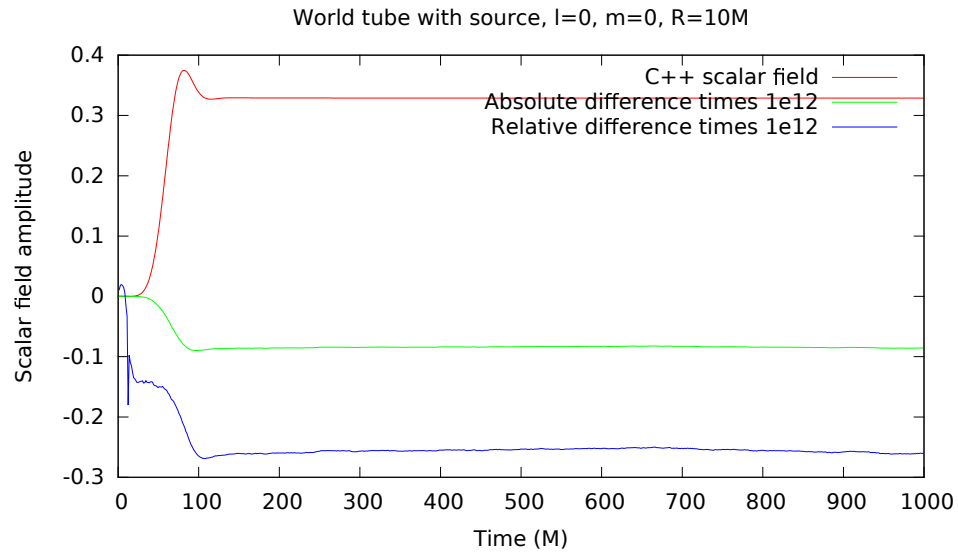
Figure 4.2: Comparison between Fortran and C++ scalar field along a line of sight for a particle on a circular orbit, l=0, m=0.

To roundoff precision, they agree, as evidenced by the near-machine-precision (10^{-15}) levels of agreement in both absolute and relative error that I achieve in Figures 4.2, 4.3, 4.4, and 4.5
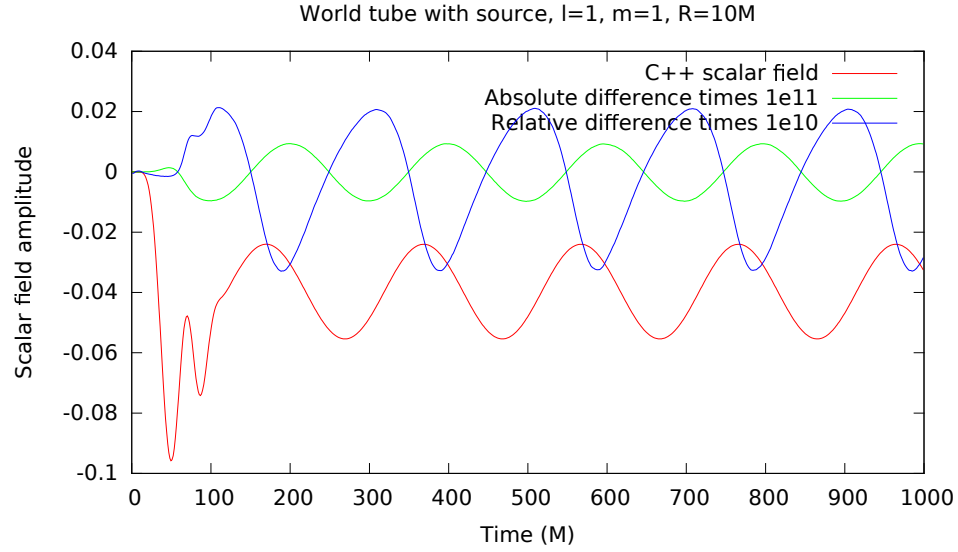
Figure 4.3: Comparison between Fortran and C++ l=1, m=1 scalar field along a line of sight for a particle on a circular orbit, l=1, m=1.
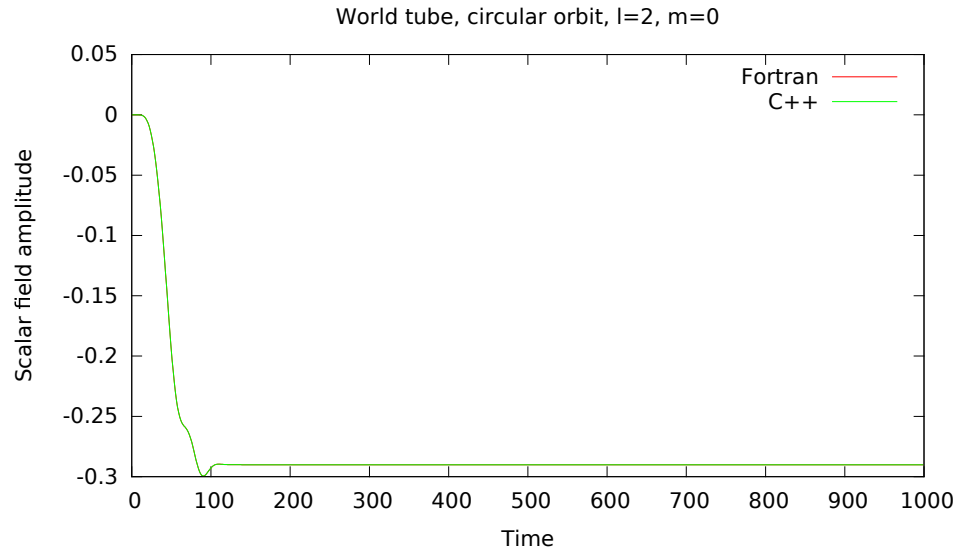
Figure 4.4: Comparison between Fortran and C++ l=2, m=0 scalar fields along a line of sight for a particle on a circular orbit, l=2, m=0.
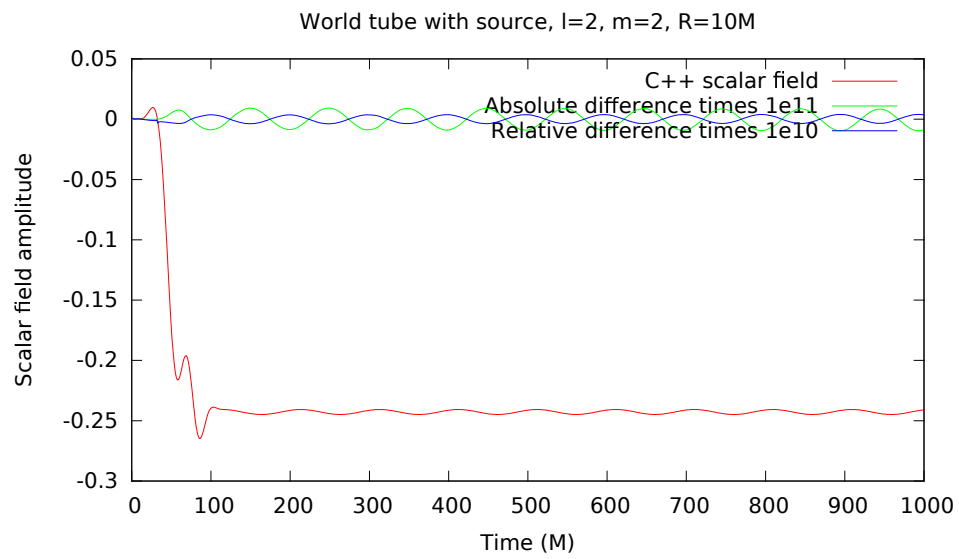
Figure 4.5: Comparison between Fortran and C++ l=2, m=2 scalar fields along a line of sight for a particle on a circular orbit, l=2, m=2.

Chapter 5
Eccentric orbits on a Schwarzschild spacetime

For eccentric orbits, there are two primary additional physical or computational effects to consider. One is the need for a way to describe relativistic eccentric orbits. The second is that in the presence of a source, it is necessary for the particle to be at an element boundary due to discontinuities in the derivatives of the effective source at the location of the particle. Discontinuities must be kept at element boundaries in the DG scheme to preserve the exponential convergence with DG order. To keep the particle at an element boundary for all times by keeping the computational coordinate fixed, it is necessary to add a time dependent coordinate transformation region between tortoise layers in the middle of the computational grid [14]. In this section, I describe Peter Diener's Fortran code, using Niels Warburton's exact initial conditions for l-modes 0 through 5, and Barry Wardell's effective source, which I have run to produce eccentric orbit output.

5.1   Orbital parameters

The eccentricity of an eccentric orbit is defined such that the turning points are defined to be $r_{periastron} = \frac{pM}{1+e}$ and $r_{apastron} = \frac{pM}{1-e}$, where p is the semilatus rectum. Eccentric orbits in general relativity precess. In the coordinates of Reference [46], χ is a parameter that runs from 0 to 2π in one radial cycle (as opposed to ϕ, which runs from 0 to 2π in one angular cycle). The orbital parameters of an eccentric orbit in a Schwarzschild space-time are derived from General Relativity to be

$$E^2 = \frac{(p-2-2e)(p-2+2e)}{p(p-3-e^2)} \tag{5.1}$$

$$L^2 = \frac{p^2M^2}{p-3-e^2} \tag{5.2}$$

For an eccentric orbit, χ and ϕ are evolved using a fourth order Runga Kutta integration using derivatives of r, χ, ϕ, and t, provided in Reference [46].

5.2 Time dependent coordinate transformation

In the case of an eccentric orbit, it is necessary to ensure that the particle always remains at an element boundary for all time. We use a time dependent coordinate transformation to keep the particle fixed at a specific coordinate location while the coordinates in its immediate neighborhood evolve. This simulates a particle on an eccentric orbit and produces the same self-force and the same scalar waves at $\mathscr{I}^+$. The necessary time dependent coordinate transformation can be found in Reference [14]. It transforms from tortoise coordinates, x, to time dependent coordinates, ξ. The location of the particle $x_p(t)$, varies in tortoise coordinates but is fixed in time dependent coordinates (ξ_p). a and b are the boundaries of the time dependent region, in computational coordinates.

$$x = a + \frac{x_p - a}{x_p(t) - a}(\xi - a) + \frac{(b - x_p(t))(\xi_p - a) - (x_p(t) - a)(b - \xi_p)}{(\xi_p - a)(b - \xi_p)(b - a)}(\xi - a)(\xi - \xi_p) \quad (5.3)$$

I have used Mathematica to confirm the time dependent coordinate wave equation used in Peter Diener's Fortran scalar self-force code. Its time and radial components, leaving out the potential term, are

$$\frac{\partial^2 \psi}{\partial t^2} = \left(\frac{\partial x}{\partial \xi}\right)^{-3} \left[\frac{\partial^2 x}{\partial \xi^2} - \frac{\partial^2 x}{\partial \xi^2}\left(\frac{\partial x}{\partial t}\right)^2 - 2\frac{\partial^2 x}{\partial \xi \partial t}\frac{\partial x}{\partial \xi} - \left(\frac{\partial^2 x}{\partial t^2}\right)^2 \right] \frac{\partial \psi}{\partial \xi}$$
$$+ \left[-1 + \left(\frac{\partial x}{\partial t}\right)^2 \right] \left(\frac{\partial x}{\partial \xi}\right)^{-2} \frac{\partial^2 \psi}{\partial \xi^2}$$
$$- 2\frac{\partial x}{\partial t}\left(\frac{\partial x}{\partial \xi}\right)^{-1}\frac{\partial^2 \psi}{\partial \xi \partial t} \quad (5.4)$$

At the world tube boundary, it is necessary to transform from one coordinate system to another before or after adding or subtracting the derivative of the singular field from the radial or time derivative of the scalar field, in order to transform between regular and retarded fields in time dependent coordinates and in hyperboloidal coordinates respectively.
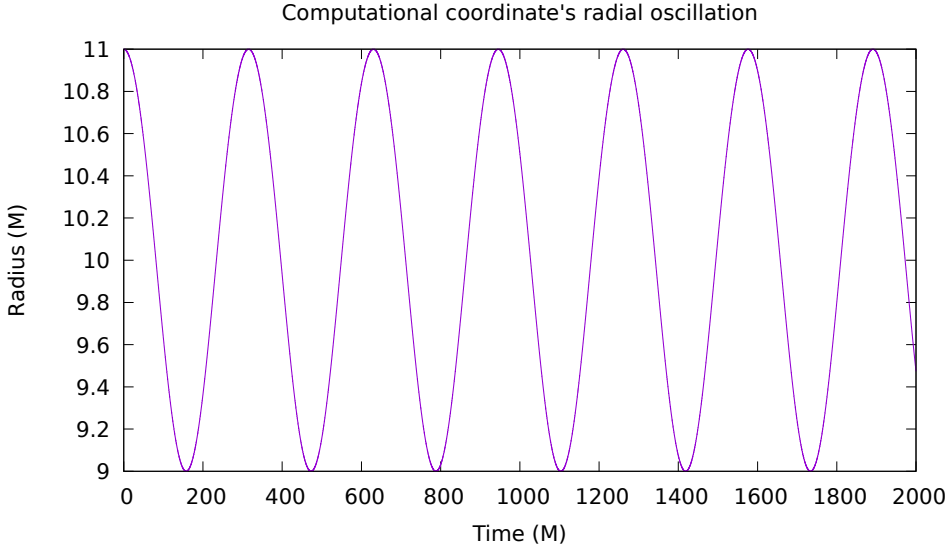
Figure 5.1: Schwarzschild r as a function of time over several orbits. $p = 9.9$, $e = 0.1$

5.3 Orbits

I have computed several orbits of the system for $p = 9.9$, $e = 0.1$. In this chapter and for the rest of this document, the waveform is extracted at the location of the particle, rather than at the radius of the particle along a fixed direction. Figure 5.1 shows the radial coordinate in Schwarzschild coordinates as a function of time. Figure 5.2 depicts the physical path of the orbit, including precession. Figure 5.3 demonstrates why precession must exist. The periods of the angular variable ϕ and the parameter that governs the rate of radial evolution, χ, are not synchronized.

5.4 Self force output

The radial self-force is defined as $q\nabla^{\alpha}\Psi^{R}$ [60]. To compute this self force, it is necessary to sum over all l and m modes. In principle it is necessary to sum to $l = \infty$. Figures 5.4, 5.5, and 5.6 are computed by displaying the first several individual l modes from this partial mode sum, summed over m.
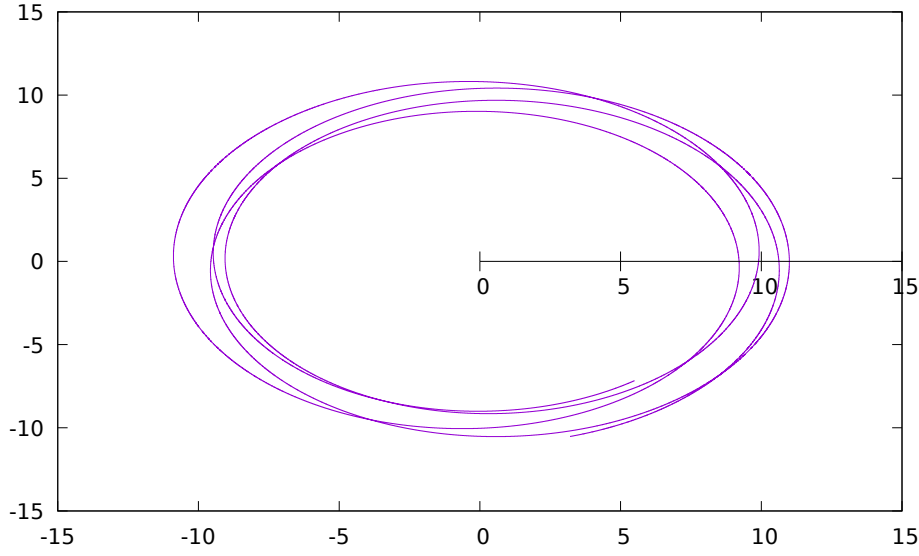
Figure 5.2: The orbit as it physically would exist, using Schwarzschild ϕ as the polar coordinate angle. The orbit precesses but does not inspiral since there is no generic evolution. Shown for $p = 9.9$ and $e = 0.1$
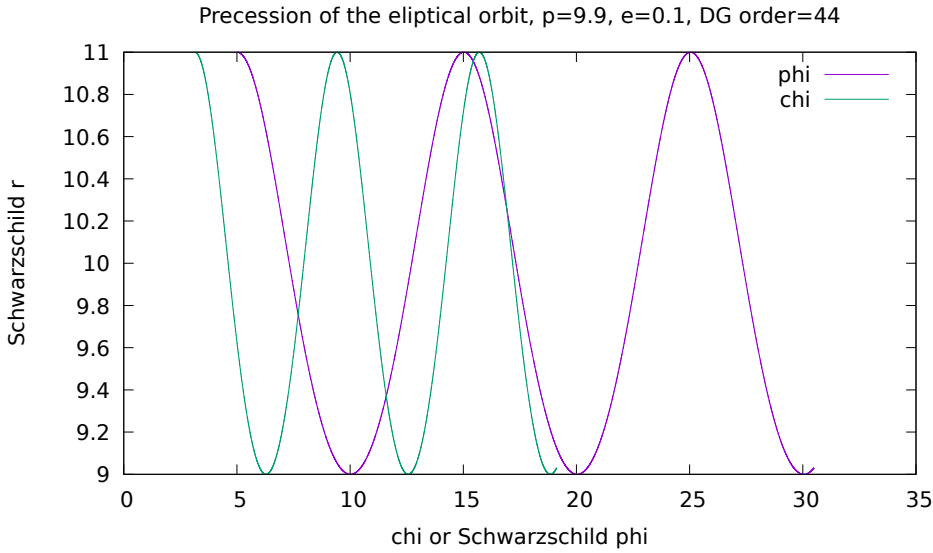
Figure 5.3: Precession of the eccentric orbit is demonstrated due to the inequality in the period of the angular variables χ, which represents the period of the radial oscillations, and ϕ, which represents the period of the angular oscillations. $p = 9.9$, $e = 0.1$

31
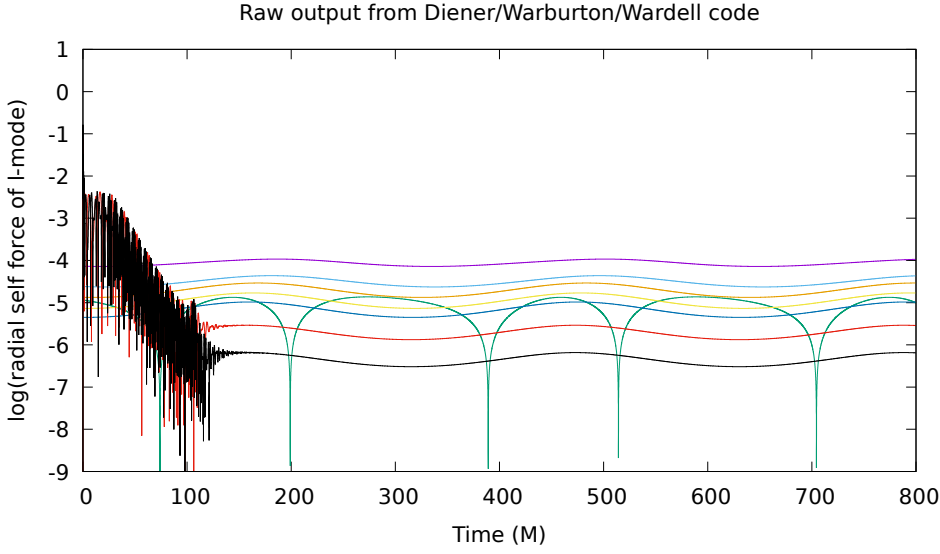
Figure 5.4: Raw output of Diener, Warburton, and Wardell code for DG order 44. Radial self force. The first several l-modes are displayed. For modes 0 through 5, Niels Warburton's frequency domain initial conditions are used to avoid transients. For modes 6 and 7, transients converge exponentially to an oscillating waveform that has a lower amplitude for higher modes.
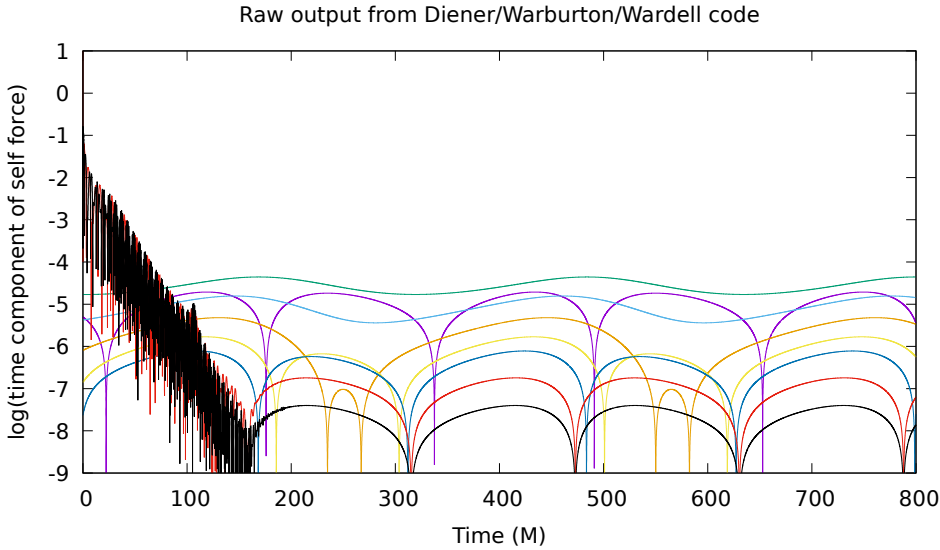
Figure 5.5: Raw output of Diener, Warburton, and Wardell code for DG order 44. Time component of the self force. The time component of the self force shares a similar behavior to the radial component with the self force.
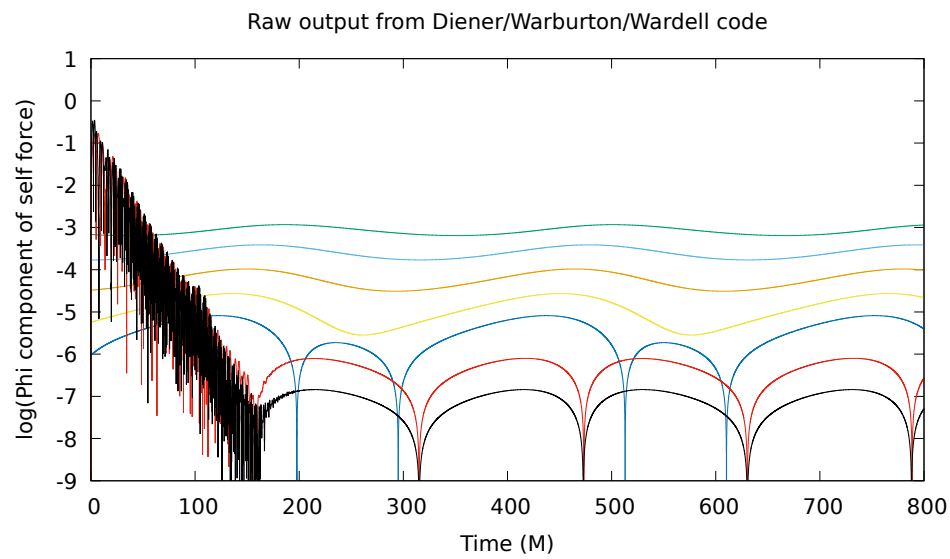
Figure 5.6: Raw output of Diener, Warburton, and Wardell code for DG order 44. Phi component of the self force. The phi component again shows this convergent behavior and the lack of transients from in the initial data from the frequency domain simulation.

Chapter 6
Extrapolating the self force to infinite Discontinuous Galerkin order

To achieve a self-consistent simulation, it is necessary to take the back-reaction into account by evolving the mass and acceleration along with the field itself. The long term goal is to perform an accurate study of the differences between the geodesic evolution method used in Niels Warburton's frequency domain technique and the self-consistent evolution method used in Peter Diener's time domain technique for the scalar approximation to the extreme mass ratio inspiral problem. Peter Diener has implemented a self-consistent simulation using Barry Wardell's self-consistent effective source that uses Niels Warburton's frequency domain initial conditions to supply steady state initial data without transients. I am running code from this simulation. Our simulation has some stability issues that must be addressed to evolve for longer durations. One possible explanation is the truncation error. Another possibility is with the sum of the l-modes. A specific functional form is fit over intermediate values of l to extend the sum analytically past the highest l-mode computed to $l = \infty$. There are uncertainties associated with the manner in which this sum is performed. In this chapter, I explore the truncation error associated with the first order Richardson extrapolation.

6.1   First order Richardson extrapolation

The Discontinuous Galerkin method results in truncation error that scales as h^{N+1}, where h is the element size and N is the order of the interpolating polynomials within the element. [21] The radial self force is given by the radial derivative of the scalar field, $F_r = \partial_r \Psi$. However, to obtain this quantity, it is necessary to sum the radial derivatives over all l and m modes. Let $F_l = \sum_{m=-l}^{l} F_{lm}$. Each of these modes, separately, follows the DG convergence scaling laws. It should be possible to extrapolate to infinite DG order based and obtain the first order Richardson extrapolation, F_{inf}, which is the self force for a given l-mode at infinite DG order after a single iteration of the extrapolation of the errors. If the Richardson extrapolation were extended to

second order, the error of the error may take on a different functional form, and the second order extrapolation may require a different technique; however, I do not perform it because there is too much random noise in the second order error to determine a functional form.

The following three-point exponential extrapolation is motivated by our assumption that Discontinuous Galerkin error is one-sided in the truncation error regime– it is not random; hence, the self force more or less monotonically approaches a limit. In the round-off error regime where the error is random, the self-force is no longer monotonically converging. As long as it is monotonically converging, the self-force at finite DG order, n, can be written in the form $F_r(n,l) = F_{inf}(l) + c(l)\exp[-\alpha n]$, where n is the DG order. For a given mode, there is a four step procedure for determining the three parameters associated with the Richardson extrapolation. A system of equations with three different DG orders using the preceding expression for $F(n,l)$ is solved for the parameters F_{inf}, $c(l)$, and α. Peter Diener originally performed this calculation with one choice of orders n_1, n_2, and n_3. I have reproduced it with the orders permuted.

$$g(\alpha) - P = \quad\quad 0 \tag{6.1}$$

$$g(\alpha) = \quad \frac{\exp[\alpha(n_1-n_2)]-1}{-1+\exp[\alpha(n_1-n_3)]} \tag{6.2}$$

$$P = \quad \frac{F_r(n_1,l)-F_r(n_2,l)}{F_r(n_1,l)-F_r(n_3,l)} \tag{6.3}$$

A root finding technique must be used to solve the following system of equations to determine the exponent of the self force. α must be greater than zero, since the self force is converging with DG order. We use the bisection method.

Secondly, the mode-dependent coefficients of the exponent must be determined.

$$c(l) = \frac{F_r(n_1) - F_r(n_2)}{\exp[-\alpha n_1] - \exp[-\alpha n_2]} \tag{6.4}$$

Finally, the first order Richardson extrapolation, the value of the self force at infinite order, to first order in the errors, depends on the l-mode and the time. The time dependence is implicit in

the time dependence of $F_r(n_3)$.

$$F_{inf}(l,t) = F_r(n_3) - c(l)\exp[-\alpha n_3] \tag{6.5}$$

Sometimes there is not a solution due to roundoff noise causing a deviation from the expected exponential behavior. In practice we allow all three parameters to vary with l-mode and time. I use extrapolation starting orders from the set 12, 16, 20, 24, 28, 32, and 36, with additional data at orders 40 and 44 that may be used as points two and three. Sets of three consecutive DG orders on this list were used. In order to use data from several different DG orders, it was necessary to interpolate between the times at which each order was computed to some desired common set of times. Each order uses different time steps for Courant stability, which requires that time steps are less than the wave travel time across the minimum spacing on the grid. Interpolation was performed using a cubic polynomial scheme.

6.2   Choice of starting order

Some modes fail because roundoff noise causes the data to deviate from exponential convergence, it is not possible to choose the same starting order for the extrapolation for all modes and all times. This can be done manually, but to produce an evolution over the entire time series to investigate the error as a function of time, it is desirable to automate this process.

6.2.1   The last non-NaN method

The first attempt I made to improve the choice of starting order was to chose the highest starting order for which no lower starting order had been unsolvable. Figure 6.1 shows this approach leads to some discontinuities in the time evolution of F_{inf} in some l-modes ($l = 3$ is shown).

- **Manually correcting badly selected automatic values**

To address this concern, I examined the choice of starting order more closely for specific times where discontinuities were present. If the DG orders converged perfectly, they would form a line in semi-log space once F_{inf} is subtracted, if it could be subtracted perfectly. See

36
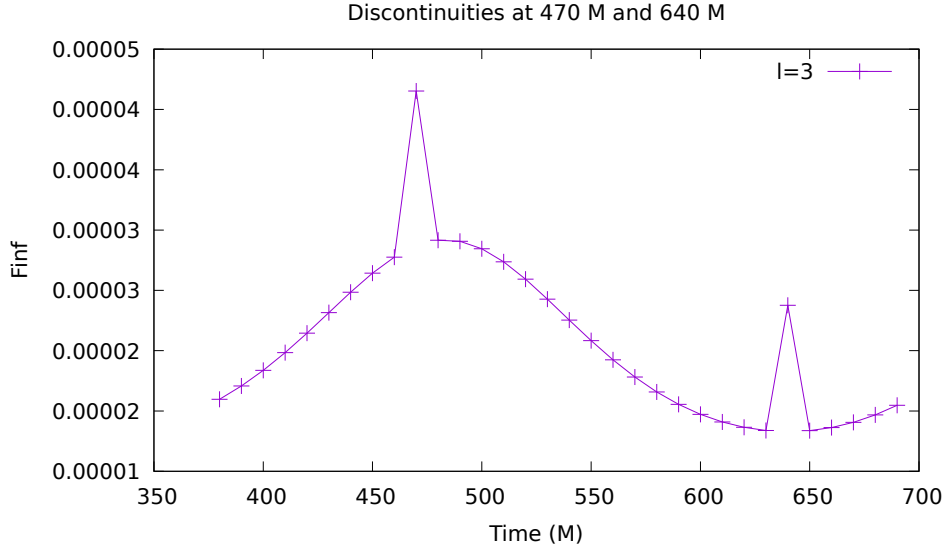
Figure 6.1: Starting order was chosen by iterating from the lowest order to the first order for which the starting order had no solution, and choosing the maximum starting order that succeeded. When F_{inf} is evolved over one full orbital cycle, some l-modes shows discontinuities at some times. l=3

Figure 6.7 for an example. Some less perfect examples are shown below. This time, $t = 632$ M, is particularly bad, which is why it produced the glitch that requires investigation. $l = 2$ and $t = 632M$, is shown in a Table 6.1. The starting orders that have solutions agree to seven digits.

Figure 6.2 shows an example where there is curvature in semilog space after F_{inf} subtraction. This could be due to second order truncation error. This effect, combined with roundoff noise in the choice of F_{inf}, is visible in Figure 6.3 at high DG orders. While it is possible that second order truncation error itself is enough to make it difficult to choose an F_{inf} correctly, I also noticed some difficulty with numerical stability at greater than the 10^{-14} level in the parameters determined using the bisection method depending on the initial values selected to bracket the interval. Since a subtraction of two nearly equal numbers is required to produce this convergence curve, roundoff error in F_{inf} is expected. Figure 6.2 also demonstrates why the extrapolation starting with DG order 28 fails– the rate of convergence does not appear to be exponentially spaced for the three points used in that extrapolation. In Figure 6.4, it is possible the effect at high DG orders is roundoff noise in the $F_r(n,l)$ values of the points, but it is more likely that it is roundoff noise in the choice of F_{inf} due to limitations of the root finding method, resulting in an incorrect offset of

37

Starting Order	F_{inf}
12	no solution
16	2.40975299617e-05
20	2.40975300465e-05
24	2.40975300114e-05
28	no solution
32	2.40975299291e-05
36	2.40975299148e-05

Table 6.1: Manual starting indices and F_{inf} values for t=632, l=2. These values agree to seven digits, when a solution is found.

the curve. Figure 6.5 shows that after selecting an average of the reasonably similar values from Table 6.1, the discontinuity in the $l = 2, t = 632M$ radial self-force becomes smooth. The values in Table 6.1 agree to seven digits, which is on the order of 10^{14}. This is comparable to the value of the self force at highest DG order, so choosing between them or averaging them properly is essential if we wish to improve upon the highest several orders available to us.

6.2.2 The median method

To resolve the discontinuity problem, I attempted another approach. I ordered the starting orders that had a solution at each time and for each mode by their F_{inf} values. The median value of F_{inf} was selected, in the hope that it will discard those effected by roundoff and those effected by failure to converge. However, there is no guarantee that it selects those in this regime, since in principle a mode could both be in the roundoff limit and have not converged yet. For comparison, see Figure 6.6 for the relative error between the minimum, the maximum, and the median, though it is not theoretically expected that the minimum or the maximum of the self force should give meaningful values over all times and all modes. See Section 6.2.4 for a more lengthy discussion of these issues. Notice that there is structure in the comparison to the minimum. This suggests that the minimum may be behaving as an asymptote for at least some modes. The reader should be aware that in the presence of random noise such as roundoff noise, the maximum, minimum, and median are all rather ill-behaved statistics, will be difficult to characterize, and may have some odd behaviors over time.
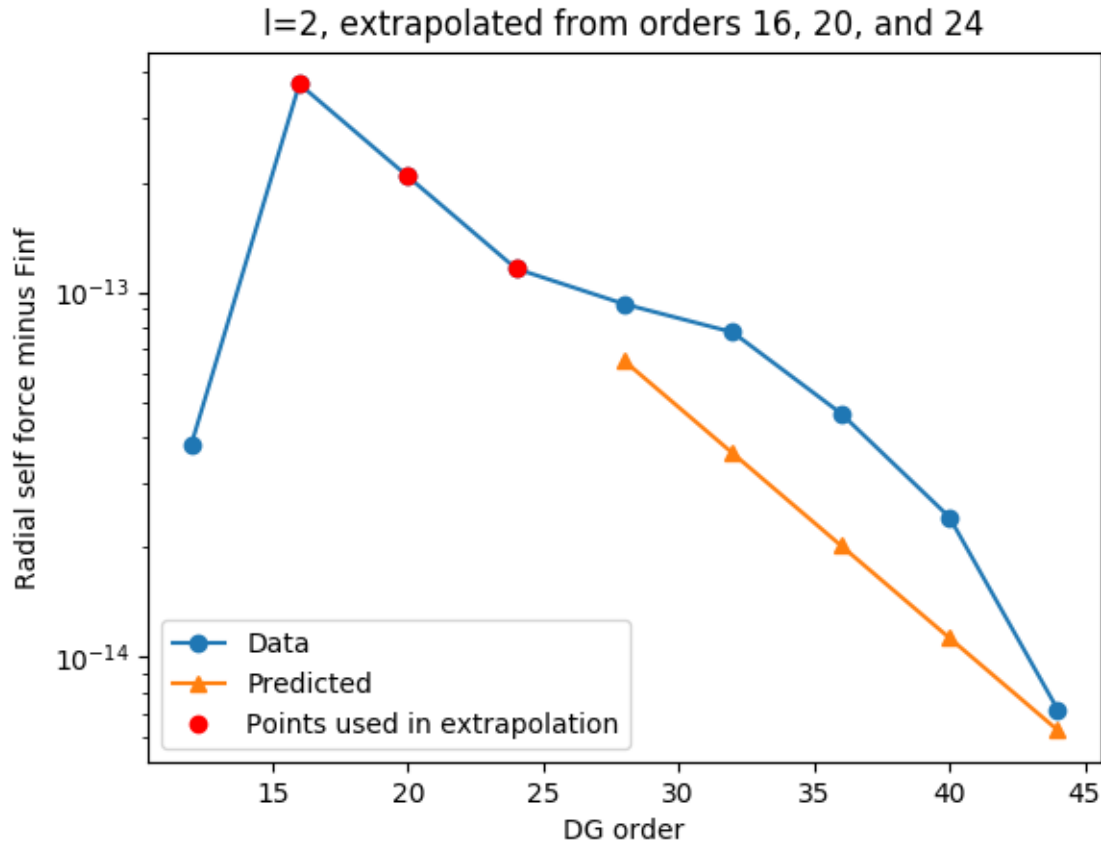
Figure 6.2: Radial self-force with F_{inf} subtracted. There is curvature in the semi-log plot after F_{inf} subtraction, most likely due to second order truncation error. t=632, l=2, starting order 16.
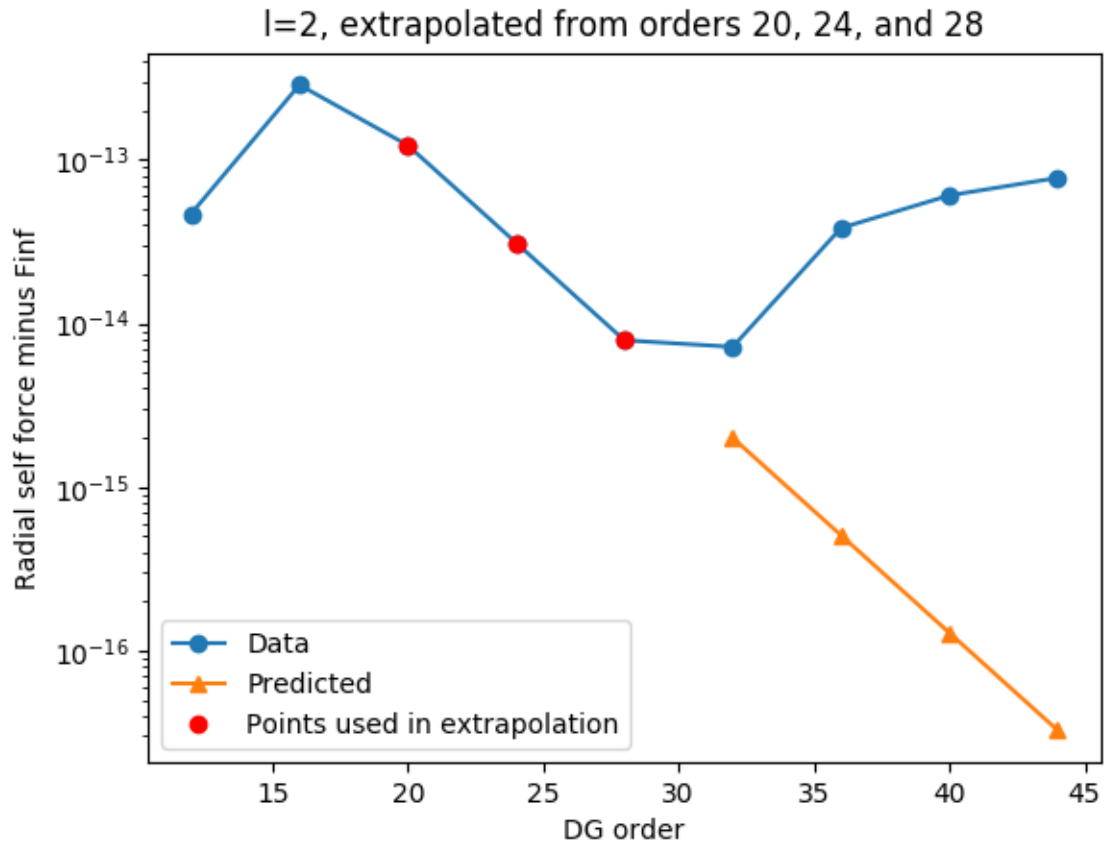
Figure 6.3: Systematic roundoff error is visible at high DG orders. This is a combined effect of roundoff error in F_{inf} selection due to limitations of the root finding algorithm and second order truncation error. t=632, l=2, i=2.
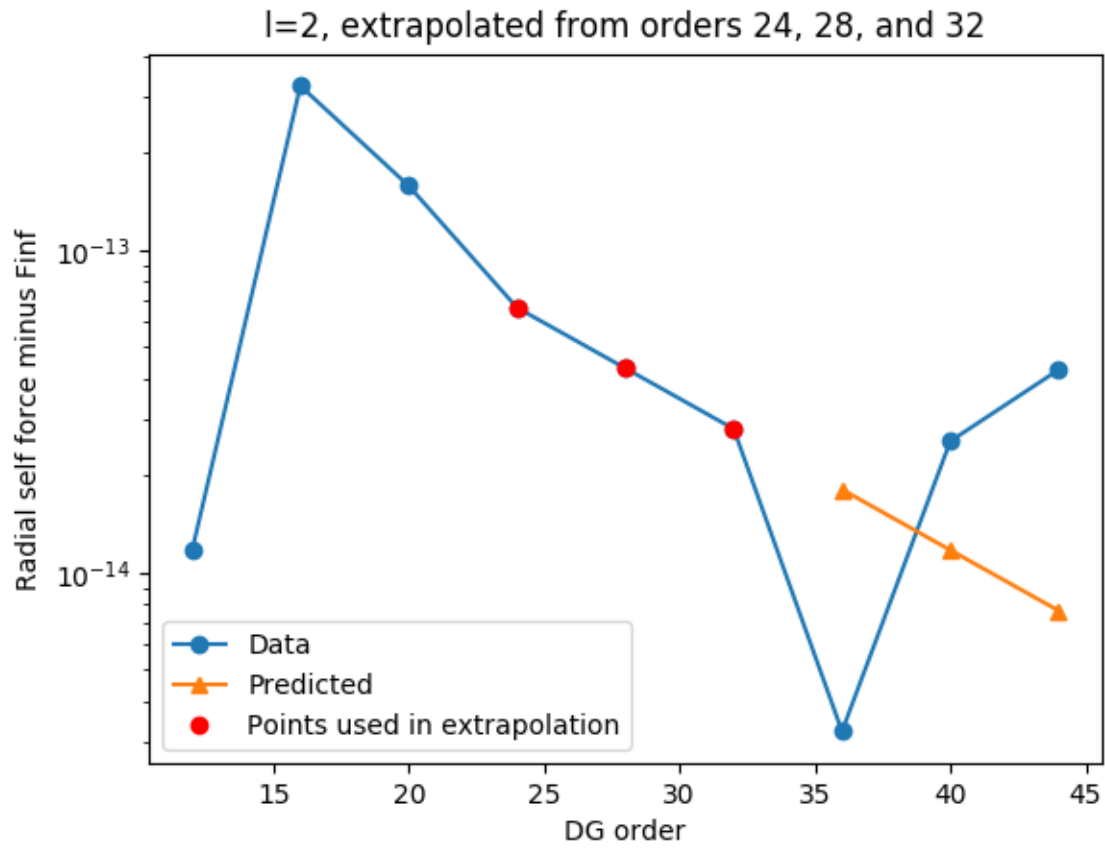
Figure 6.4: Radial self-force with F_{inf} subtracted. At high DG orders, roundoff error is visible. t=632, l=2, starting order 24
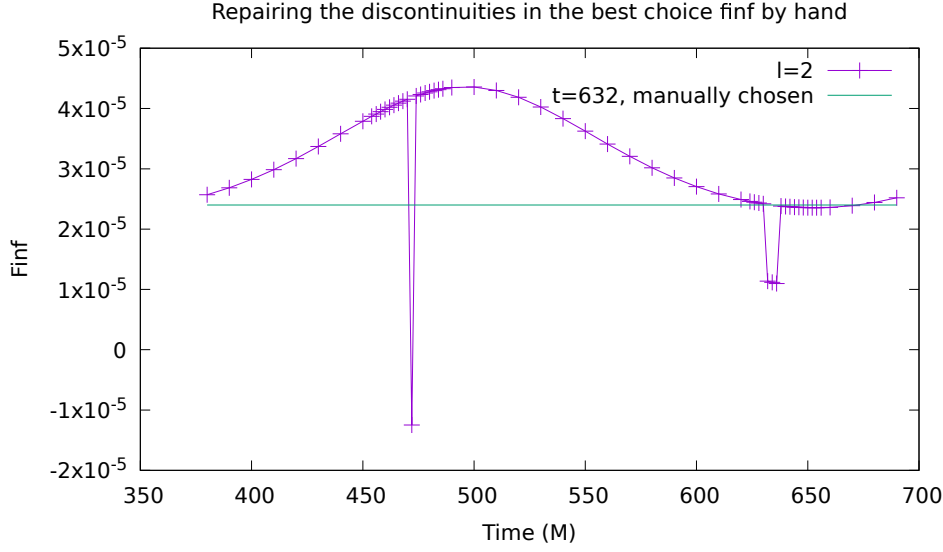
Figure 6.5: F_{inf} as a function of time. Manual correction for discontinuities in the l=2 mode, using the manually determined F_{inf} data from Table 6.1.
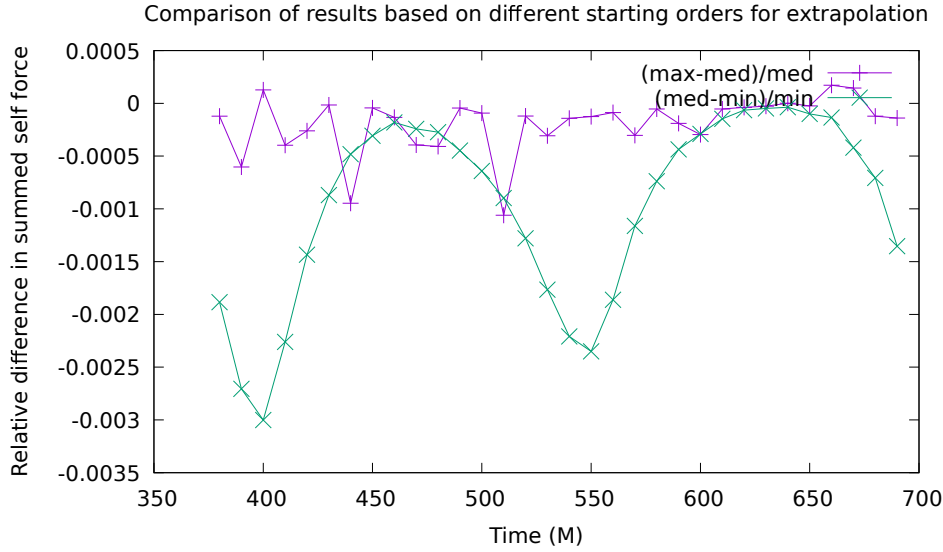
Figure 6.6: This is the relative error in the best choice self-force selected by the median method compared against the self force selected by taking either the maximum (purple) or minimum (green) of the available non-NaN self-force values over all DG orders. This uses the three term mode sum discussed in Chapter 7.4 to obtain a sum over all l-modes and to extend the sum to $l = \infty$.

6.2.3 The fit method

A better motivated approach, is to fit subsegments of lines in semi-log space on the DG order convergence plot, and find the longest and most linear region. A fit with the "best" value of the reduced chi squared should be a good approximation to this. The reduced chi squared is the value of the sum of the residuals of the fit squared divided by the number of degrees of freedom, which in this case is the number of points in the fit minus two, since there are two degrees of freedom in a linear fit. The expectation value of the reduced chi squared, in the limit of a large number of degrees of freedom, is one. I loop over starting and ending points of the fit, and over starting orders, and choose the starting order with the best fit line segment in the sense that that line segment has a reduced chi squared closest to one. An example of such an automatically chosen starting index is given in Figure 6.7, where there is a long exponentially converging region. Figure 6.8 shows that the absolute error between fit and median techniques increases with l-mode, possibly indicating that roundoff error becomes a more significant factor in the median technique as the l-mode increases, and the fit technique should perform better than the median technique.

The absolute error between the fit and median methods increases with l-mode suggesting that roundoff error becomes more important at higher l-modes.

There are some outstanding issues with this method. Specifically, I am concerned about the normalization of the the reduced chi-squared, given the unspecified normalization of the second order errors; however, this doesn't seem to prevent the algorithm from nearly working, so perhaps the normalization is nearly correct by chance. Secondly, the fact that the three points used in the extrapolation on the self-force minus F_{inf} curve are precisely on a line in semi-log space means that any hypothesis test is going to be skewed to preferentially select regions including only those three values. To correct for this, it might be better to consider a statistic based upon residuals to the parameters obtained by the extrapolation, with the number of degrees of freedom adjusted to account for the three fixed points. The second order noise is plainly not Gaussian or even unbiasedly distributed, so it is not simple to calculate an expectation value for such a statistic;

43
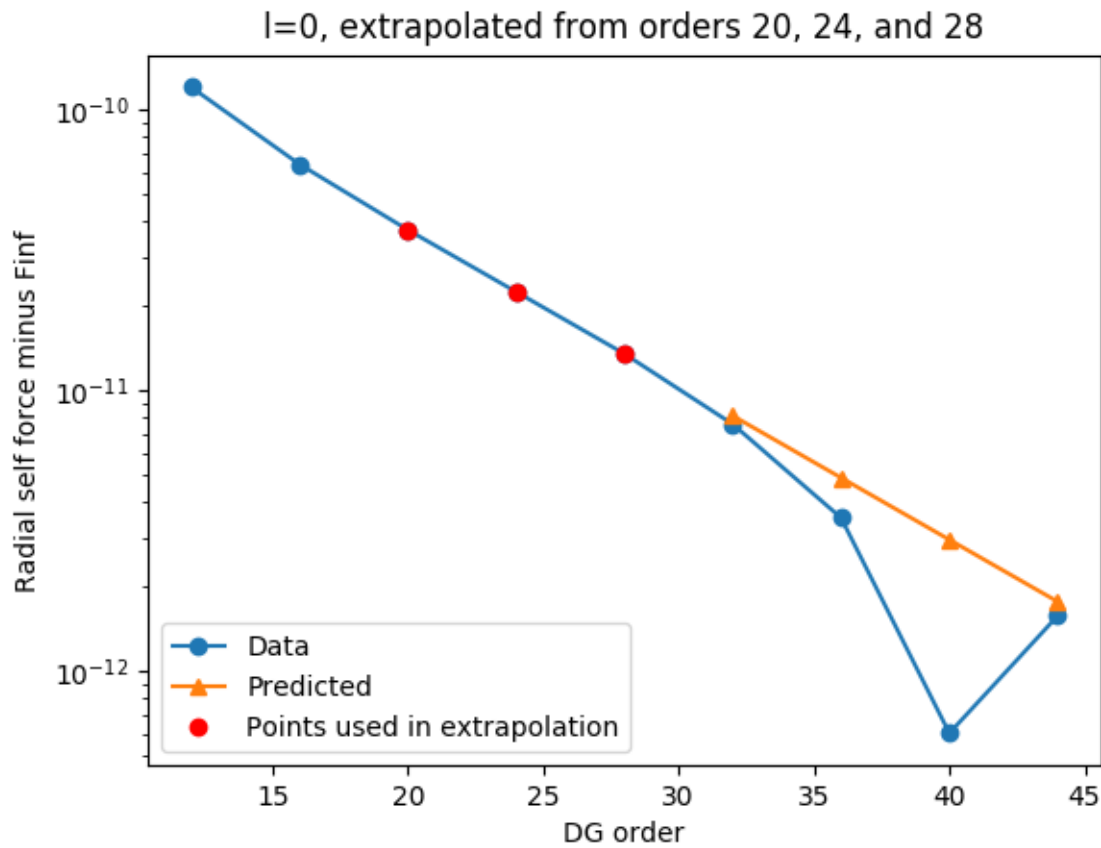
Figure 6.7: l=0 mode with line-segment fit-chosen starting order produces convergence plot with long exponentially converging region
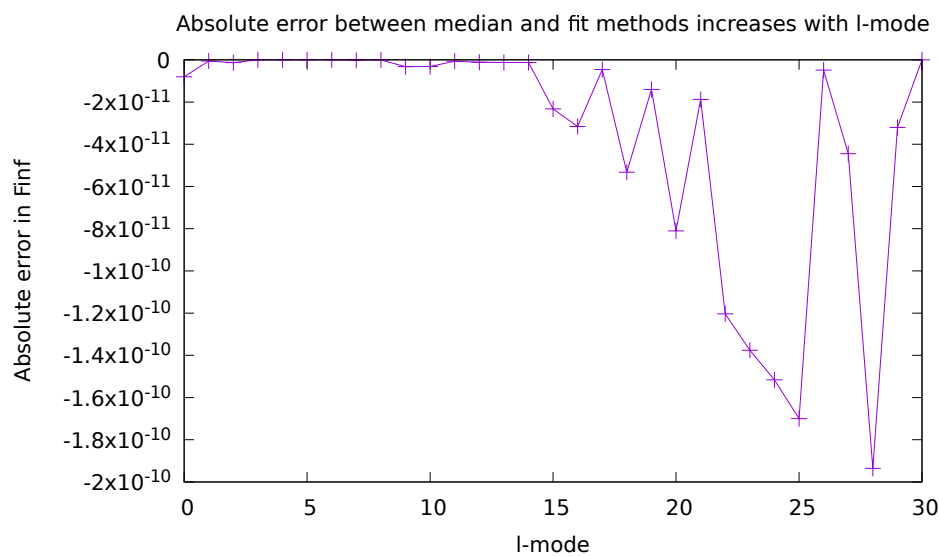
Figure 6.8: Absolute error between fit and median techniques increases with l-mode.

however, it should have properties similar to the reduced chi squared, so in a back-of-the-envelope sense, can probably be compared to that statistic with the appropriate choice of the degrees of freedom. The biased nature of the second order truncation error is also an issue when using the chi squared test in its usual form.

6.2.4   The asymptote method

In a fourth approach, I consider the behavior of F_{inf} as a function of starting order of the extrapolation. In many, but not all, modes, F_{inf} appears to converge to an asymptote from above or below as the DG starting order increases. However, in many modes, some starting orders produce no solution, so our set of six DG starting orders is reduced to somewhere between three and five. There are two obvious ways to test for convergence: fit an exponent or a power law and do a likelihood ratio test relative to a constant (since the second order errors are unmodelled), or, more reasonably, examine the signs of the first and second numerical derivatives with respect to DG order and consider the end of the convergent regime to be the point where the roundoff noise dominates, and the product of the sign of the derivatives becomes positive. From this derivative sign test, we can determine the best starting order for F_{inf} of a pattern of five or six points that are behaving in a converging like pattern.

However, sometimes, due to high roundoff noise or non-convergent behavior, a low DG order is chosen even for the case where there are five or six good contiguous starting indices. In that case, the asymptotic value of F_{inf} at high DG orders is under-estimated. To achieve a better estimate, I sort this group into the same class as the two, three, and four length contiguous sets of successful DG orders that generated values of F_{inf}. For this case, I make an assumption that except for one or maybe two outliers, F_{inf} is approximately constant across the range. The outliers may be at the beginning or the end, or may be due to roundoff noise fluctuations. To reject outliers, I do a standard statistical test of taking the average, making a veto based on the number of standard deviations a point is away from the average, and taking an average again using only the data that survived the veto. I select the point with the value closest to the second average as the best starting order for the extrapolation, and the value I will use to obtain F_{inf}. In

45

this case, I found that I got linear curves of $\Psi_r - F_{inf}$ on a semi-log scale for a one sigma veto.

After performing this selection of the best starting order, based on methods to look for asymptotes or reject outliers, I obtained the time evolution of the radial self force, summed from $l = 0$ to $l = 30$, shown in Figure 6.9. The absolute error between F_{inf} and the different DG orders is shown in Figure 6.10 and the relative error is shown in Figure 6.11. There is one time where there is some kind of glitch in F_{inf} that remains to be investigated; however, the evolution as a whole appears to be smooth. The absolute and relative error demonstrate that convergence is exponential until about DG order 36 or 40, and which point roundoff noise takes over. The best order for evolutions is therefore DG order 36. The spike is due to $l = 25$ at $t = 630$, where there is no starting order for which a solution exists. We have examined the time series data and there appears to be some truncation error in mode 16. There also appears to be some roundoff error in $l = 25$ at $t = 630$, though I have not yet compared it to other times. The truncation error in $l = 16$ does not explain the lack of solutions in the extrapolations starting from higher DG orders. The roundoff noise might provide an explanation for this problem, but needs further investigation. The relative error due to our inability to use a Richardson extrapolation in real time is at the level of 10^{-4} (see Figure 6.11).

Although the asymptote method has the best theoretical motivation of the four methods, we do not have sufficient data to implement it in the ideal manner. The fit method might be the next best motivated method, but it has some remaining issues. These methods are currently under development and this chapter has largely been arranged chronologically. We plan to continue to develop these algorithms using some combination of the asymptote method and the fit method.
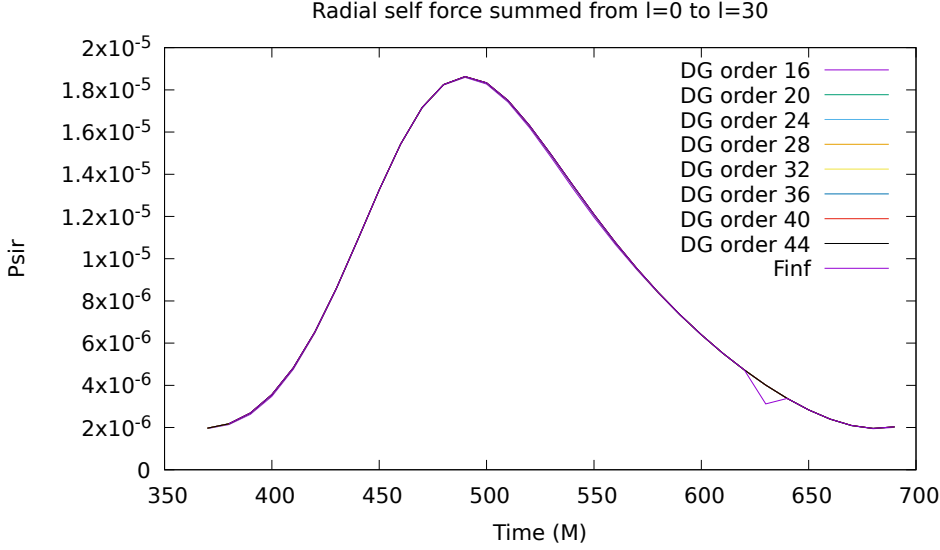
Figure 6.9: Sum from $l = 0$ to $l = 30$ of the radial self force, comparing all DG orders to F_{inf}. This was obtained using the method based on asymptotes and averages with rejection of outliers.
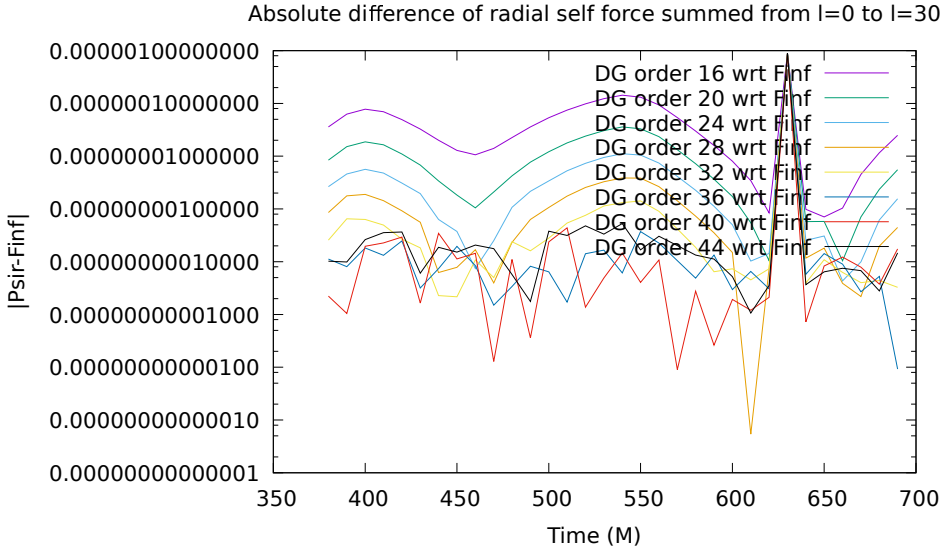
Figure 6.10: Absolute difference of the radial self force summed from $l = 0$ to $l = 30$ for each DG order compared to the total radial self force for these modes for F_{inf}. This was obtained using the method based on asymptotes and averages with rejection of outliers.
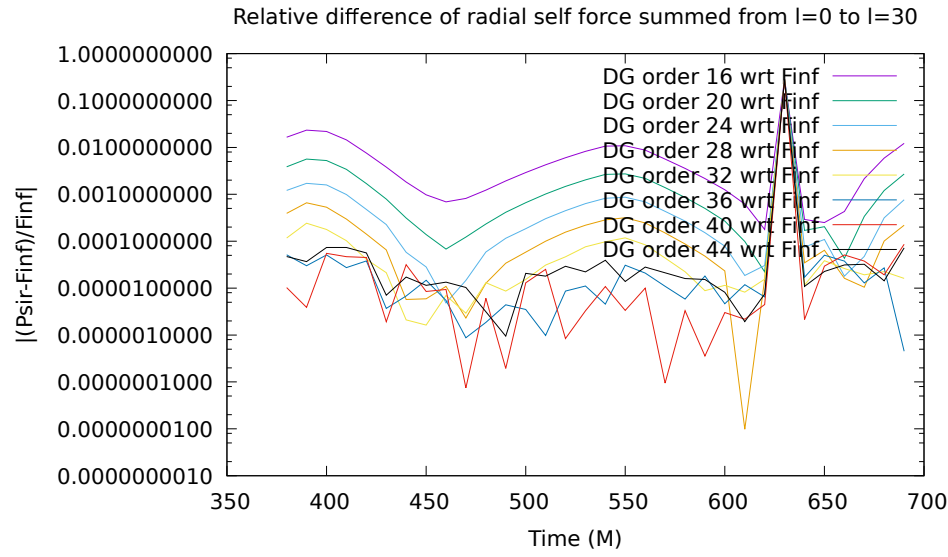
Figure 6.11: Relative difference of the radial self force summed from $l = 0$ to $l = 30$ for each DG order compared to the total radial self force for these modes for F_{inf}. This was obtained using the method based on asymptotes and averages with rejection of outliers. The error is at the 10^{-4} level.

Chapter 7
Extending the mode-summed self-force to include contributions from an infinite number of spherical harmonic modes

Note that in this chapter, the optimal method for selecting F_{inf} has not necessarily been used to produce all plots or all conclusions. That is a subject for later exploration and refinement.

In the last chapter, ψ_l was defined as the sum over m within a specific l-mode. To obtain the total self-force, it is necessary to sum all of these l-modes, for every time, using the value of F_{inf} selected for that mode. Naively, one might sum only those modes for which there is data–only up to the maximum l-mode computed in the simulation. However, it is possible to do a fit to a functional form found in Reference [20] and use the analytic sum of that functional form to add the contribution from $l_{max} + 1$ to infinity to the results computed from the simulation. The dependence of the m-summed self-force for a given mode on l, for large l, is shown below, modified to omit terms that are rescaled to zero by the definition of the effective source in [60].

$$F_r(l,t) = \quad \frac{A(t)}{(2l-1)(2l+3)} + \frac{B(t)}{(2l-3)(2l-1)(2l+3)(2l+5)}$$
$$+ \frac{C(t)}{(2l-5)(2l-3)(2l-1)(2l+3)(2l+5)(2l+7)} + \cdots \tag{7.1}$$

Here $A(t)$, $B(t)$, and $C(t)$ are constants with respect to l determined by a least squares fit. Least squares fits minimize the sum of the squared differences between the function and the data in the y direction, over all values of x_i. For fit parameters A, B, and C, and $l_{max} = n - 1$, the portion of the total radial self-force contributed by the l-modes extrapolated to infinity after the end of the known data is given by

$$\sum_n^\infty F_r(l) = \quad \frac{An}{4n^2-1} + \frac{Bn}{3(9-40n^2+16n^4)}$$
$$\frac{Cn}{5(2n-5)(2n-3)(2n-1)(2n+1)(2n+3)(2n+5)} + \cdots \tag{7.2}$$

Although Peter Diener's Fortran code implements this sum, I have analyzed it in an independent way to establish choices of l_{min} and l_{max} and to establish best choice DG orders for the code. In my computations, I have terminated the "end of the known data" at the end of the fit region, on the theory that I am simulating having more or fewer total l-modes available to me by including more or fewer l-modes in my fit.

7.1   Fitting techniques and choice of starting mode

A good fit should not have a systematic deviation to one side of the data. Such systematic deviations are often introduced in power-law fits in experimental data because the error stays about the same as the value decreases. Thus, constant errors are used in the fit, and data with a weak signal is given less importance.

However, it is difficult to apply this expectation to data in the truncation error regime of data generated from a numerical simulation. There are two differences. One is that the error is biased. While a good fit should still pass through the middle of the data in some sense, the truncation error may result in systematic deviations of the functional form of the self-force with l-mode. We believe we have corrected this to first order using a Richardson extrapolation, but higher order deviations may remain.

Secondly, the second order error is not necessarily expected to remain constant with l-mode. Ideally one would do a second order Richardson extrapolation to take the second order error into account and compute the truncation error, but our data is too sparse in starting orders with solutions. Instead, I assume the error is random and scales in two different specified manners, σ^{-1} and σ^{-2}. This is neither the classical manner of computing the roundoff noise nor the truncation noise; however, it should improve a least squares fit and therefore improve stability and accuracy in the simulation.

In these fits, I minimize the classic χ^2 with weights, as follows

$$\chi^2 = \sum_i \frac{(y_i - f(x_i))^2}{\sigma_i^2} \tag{7.3}$$

Since the σ_i weights do not represent proper statistical uncertainties, the normalization of the weights is unimportant, unless they are used to interpret the "goodness" of a fit in terms of a reduced chi-squared. Since the error behaves in an unknown, possibly highly correlated, deterministic, manner, cation is warranted in doing so. I have examined weights that are constant (effectively no weight), that scale as l^{-2}, and that scale as l^{-1}. The first is motivated by standard fitting techniques and is the default solution, while the second is motivated by the nature of the first order scaling behavior of the function to which we fit the l-modes, and the third is motivated by the desire to find something that behaves well in both the truncation error and roundoff error regimes. Figure 7.1 shows the functional form of the l-mode fit with three different choices of weights. Figures 7.2 and 7.3 show that for all choices of weight scaling, a starting l-mode of 14 is a reasonably good fit, while significantly lower starting modes are a bad fit for three terms in the l-mode fit expansion. These figures also show that the choice of sigma can make a small difference in the goodness of the fit at high l-mode, which is important for extrapolation to infinite l-mode. However, Figure 7.1 shows that for a range of l_{min} versus l_{max}, the variation in the total radial self force due to variation over start and stop range in the fit is small compared to the variation between between l^{-2} scaling and constant scaling (circles and triangles).

7.2 Roundoff noise and choice of end mode

In Figure 7.5 roundoff noise is evident at higher l_{max} choices, where l_{min} is the minimum l-mode included in the fit and l_{max} is the maximum l-mode included in the fit. This is most true of times near apastron. Note that there is not a large difference between two and three terms, and that four terms is less smooth a surface, suggesting that it is more subject to variations in the fit due to a poor fit at high l. The systematic deviations in the plot are correlated because all regions to the right of mode 27 include mode 27 in the fit, for example. The upsurge at high l is most readily attributed to roundoff noise. In Figure 7.6, a smaller region of l_{min} versus l_{max} space has been chosen to form the surface plot where roundoff noise is excluded. Three terms is preferred due to its stability within this region.
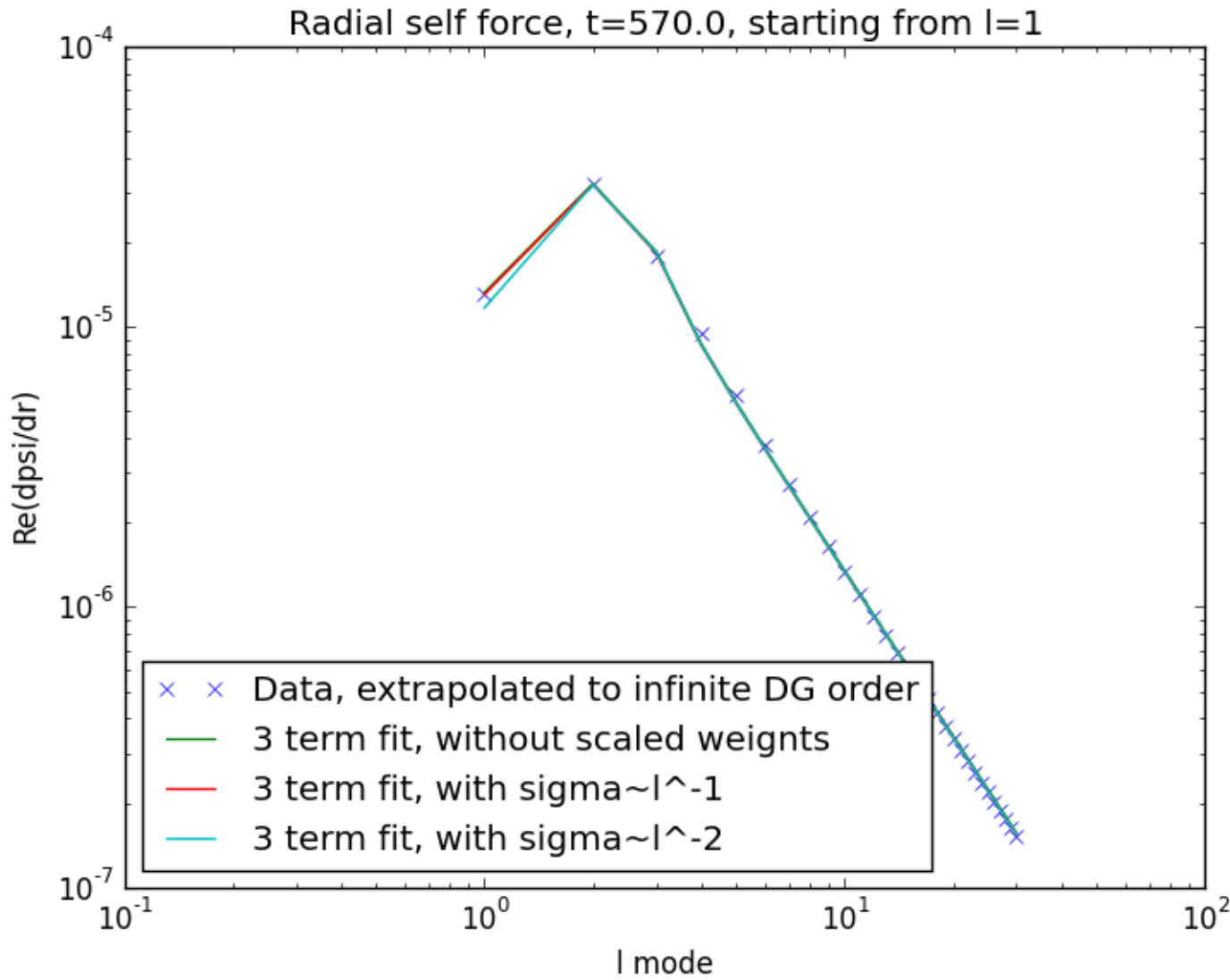
Figure 7.1: The l-mode convergence behavior and three different fits to it using three terms in the l-mode fit sum of Equation 7.1. The three different fits represent different choices of weights in the least squares fit.
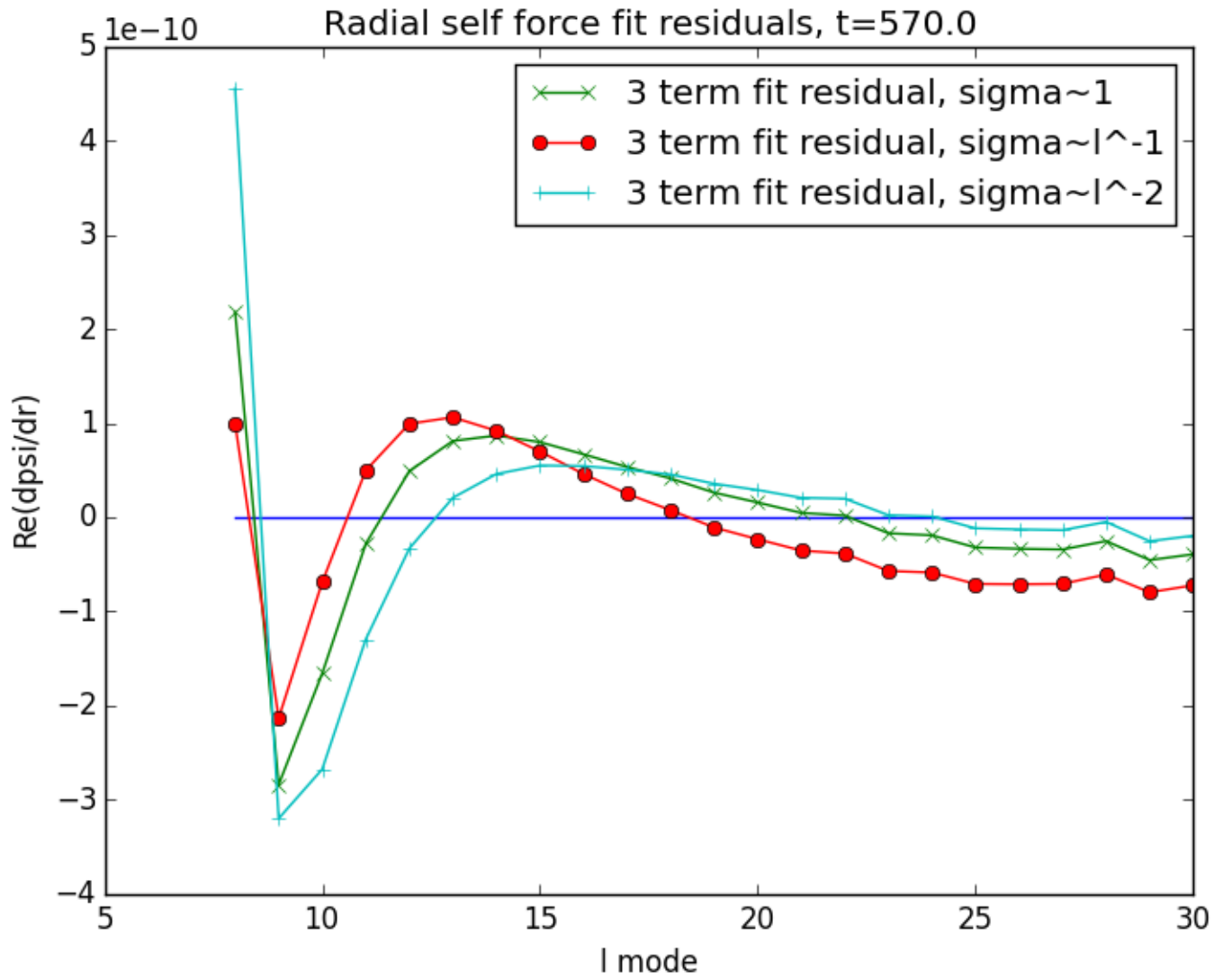
Figure 7.2: Fit residuals for three different least squares weight scalings starting from $l_{min} = 8$ to $l_{max} = 30$. Notice that this is a bad fit, due to the strong correlated skews to either side of the axis.
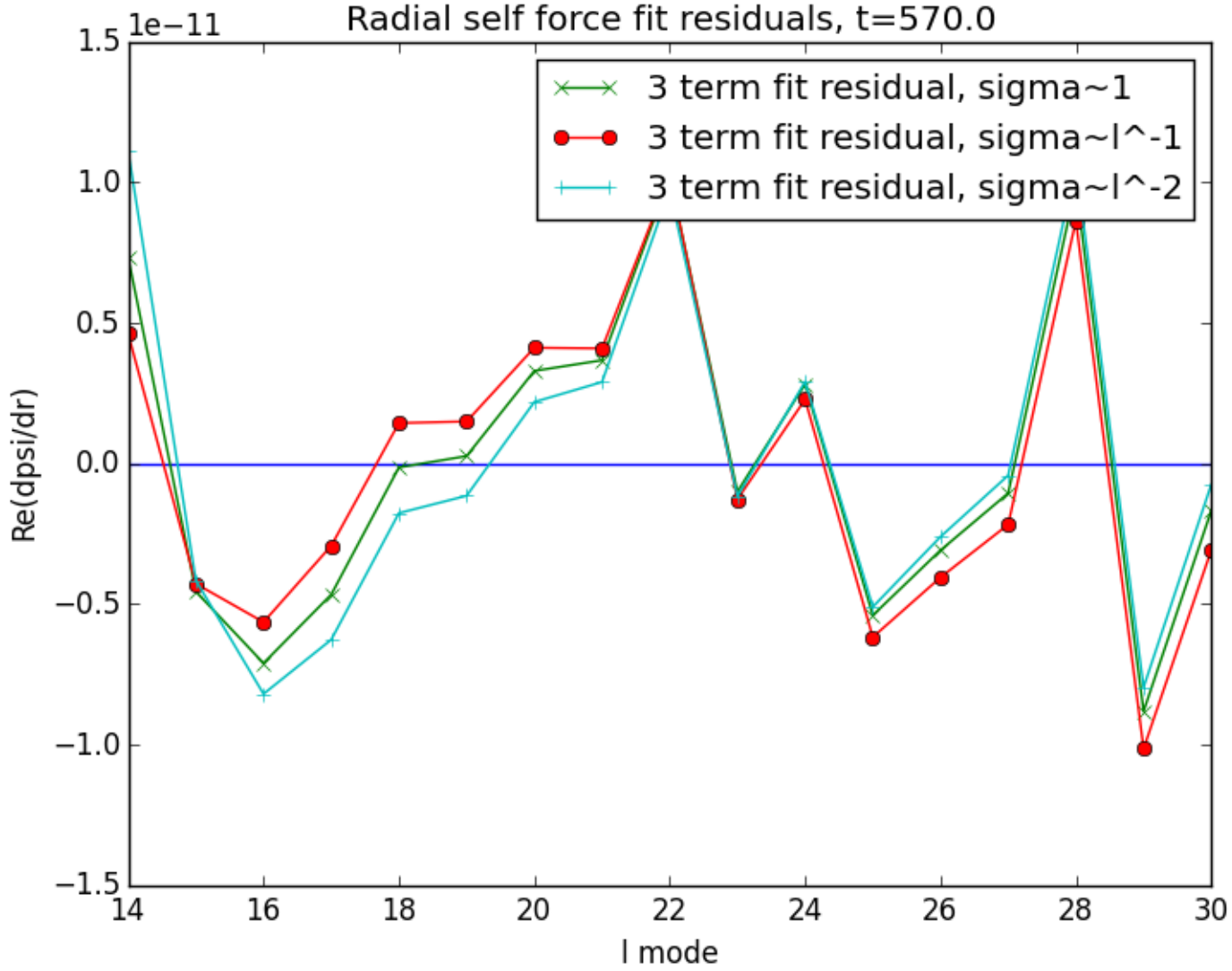
Figure 7.3: Fit residuals for three different least squares weight scalings starting from $l_{min} = 14$. This is a much better fit than $l_{min} = 8$ to $l_{max} = 30$ both due to the smaller correlated deviations from zero and due to the smaller amplitude of the residual.
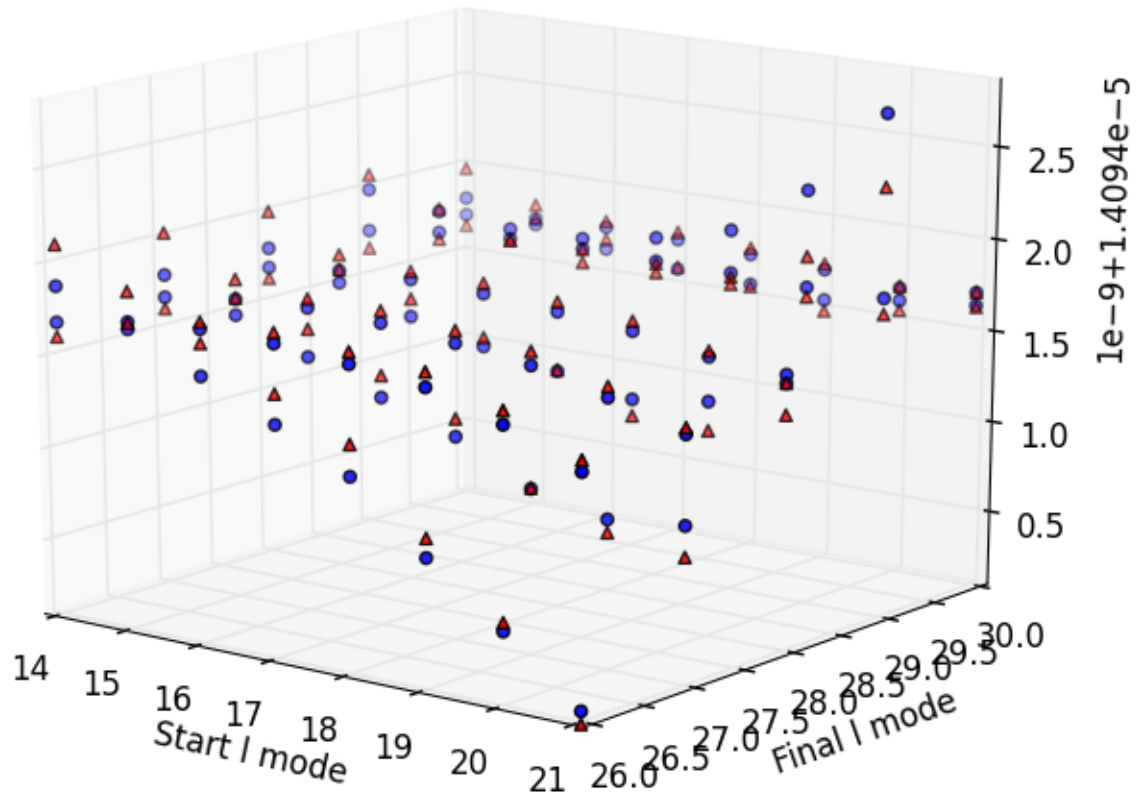
Figure 7.4: The difference between the triangles and the circles shows that the difference in the total radial self force between the presence of a $\sigma \sim l^{-2}$ weight and no weight is unimportant compared to the difference in the total radial self force between various start and end points of the l-mode fit.
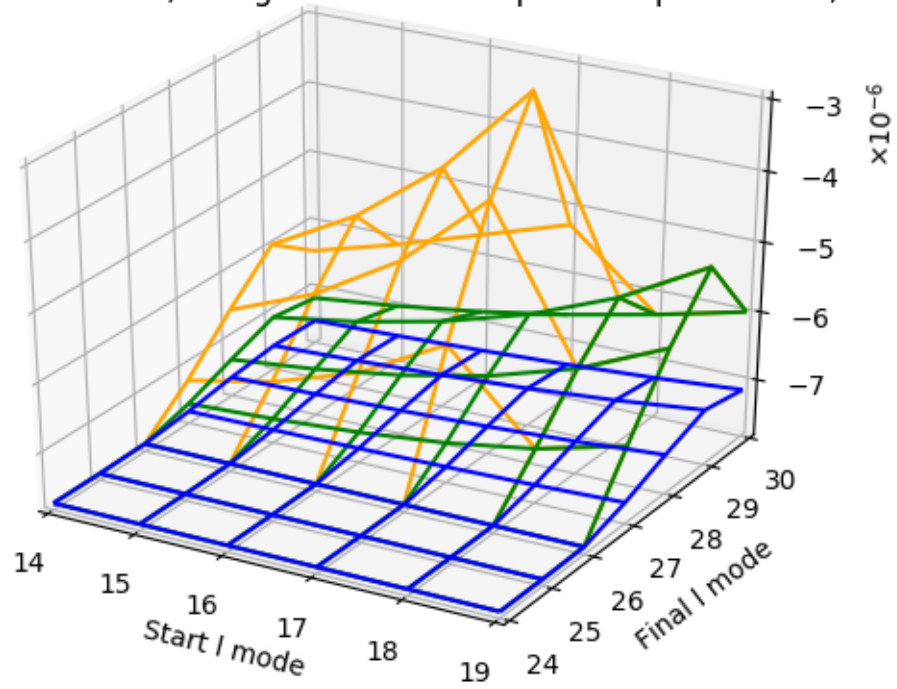
Figure 7.5: A surface plot of F_{inf} generated using the median method, t=635, 2, 3, and 4 term fits over a broad range of l_{min} and l_{max} values. Note the roundoff noise at high l_{max} that creates an upsurge in the surface. This is at apastron, where the roundoff noise effect is strongest. 2 is blue, 3 is green, 4 is orange.
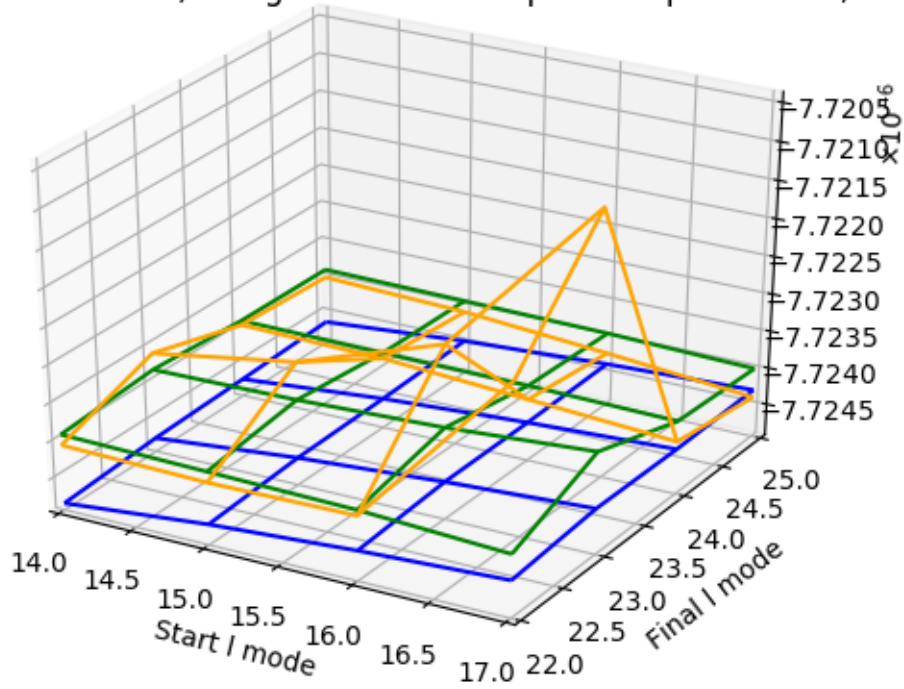
Figure 7.6: A surface plot of F_{inf} generated using the median method. t=635, 2, 3, and 4 term fits over a small range of l_{min} and l_{max}. This is near apastron where the roundoff noise is a dominant effect in the larger range of l_{max}. No roundoff noise is evident in this range of l_{min} and l_{max} so it is a suitable range to consider at all times. 2 is blue, 3 is green, 4 is orange
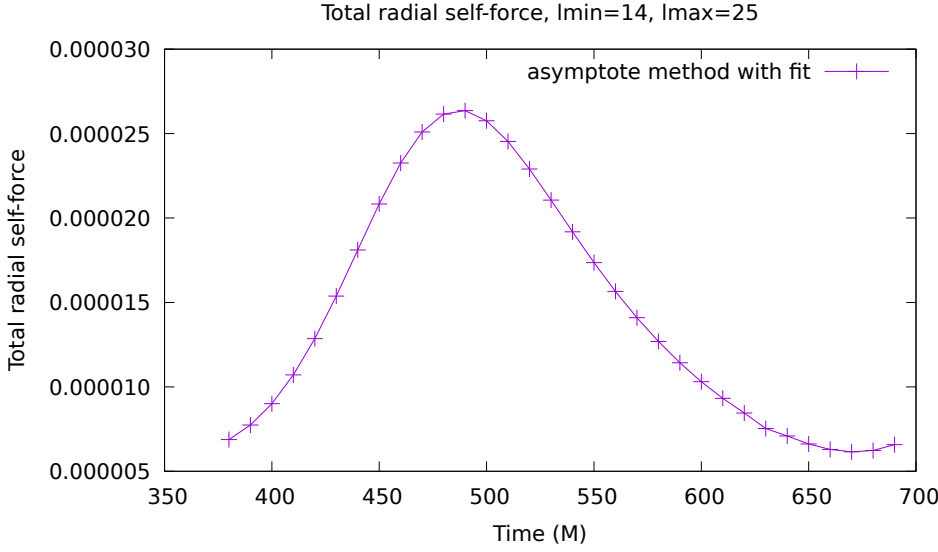
Figure 7.7: This is the total radial self force calculated using a l-mode sum including a contribution directly summing F_{inf} from $l = 0$ to $l = 25$ and a contribution obtained using an analytic sum of the three term fit in Equation 7.1. F_{inf} is measured using the asymptote method defined in Chapter 6 for selecting the best starting order

7.3   Results and errors

Figure 7.7 shows the evolution of the total self force over time using $l_{min} = 14$ and $l_{max} =$ 25. First it has been extrapolated to obtain F_{inf} using the three-point DG order exponential convergence extrapolation technique, and the optimal starting order has been chosen. Then the modes computed in the simulation have been summed numerically from $l = 0$ up to some l_{max}, and a fit from l_{min} to l_{max} has been used to extrapolate the sum to infinite l, to obtain the total radial self-force, at each time.

7.3.1   Relative and absolute differences

Figure 7.8 shows the relative difference between the total radial self force measured in two different ways. The self-force values in each surface plot shown in Figures 7.5 and 7.6 were averaged to obtain better estimates of the total radial self force as a function of time. This plot shows the relative difference. I use averages and standard deviations of correlated data with biased errors of data that is not fundamentally random, so they cannot be interpreted in the strictest of statistical senses; however, they should still provide some indication of the central value and
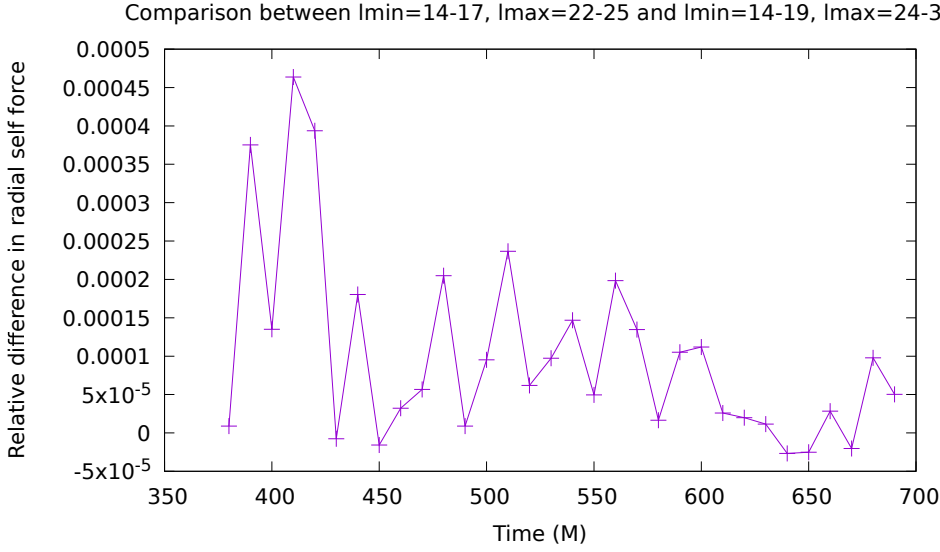
Figure 7.8: The relative difference between total self force determined by averaging large versus small ranges of total radial self-force l_{min}, l_{max} surfaces, as a function of time is at the 10^{-4} level.

spread of the data.

The relative difference introduced by the starting and end point of the fit is on the order of 10^{-4} based upon these averages. If individual modes were considered rather than averages, we might expect to see the resolution decrease by a factor of the square root of the ratio of the size of the two regions being averaged, due to the central limit theorem. That's a factor of $\sqrt{7 \times 64 \times 4} = 1.6$, which is not significant on the scale of four orders of magnitude.

Figure 7.9 shows the relative difference between using two and three terms in the fit to compute the total radial self force, as a function of time. Again, this is random, decreasing with time, and at the 10^{-4} level.

The error due to the choice of the number of terms in the fit is comparable to the error due to the choice of start and end modes and the error due to our inability to use a first order Richardson extrapolation in real time. These errors are all at the level of a relative error of 10^{-4}. The error due to the choice of fit method, visible from the offset between the triangles and circles, corresponding to the use of weights and no weights, can be seen in Figure 7.1 and is subdominant to the error introduced by the choice of l_{min} and l_{max} by at least an order of magnitude.
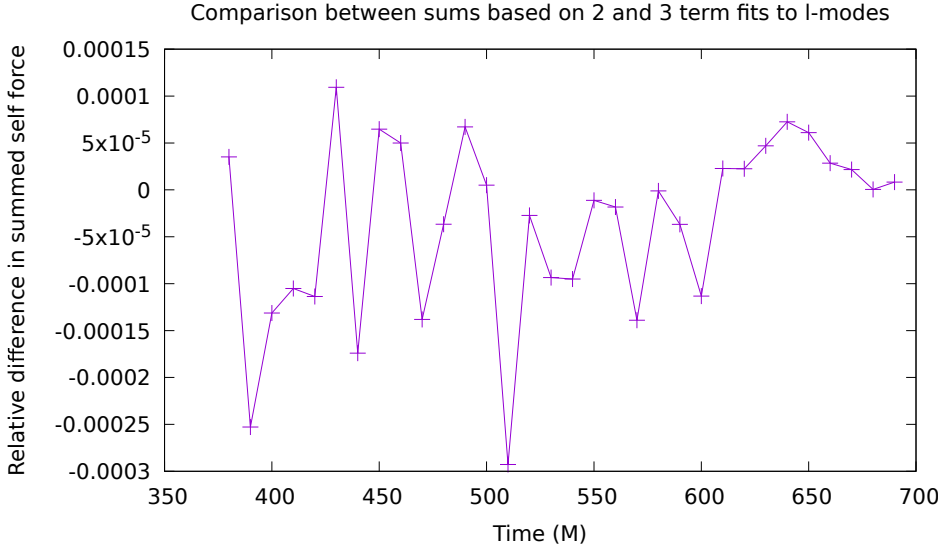
Figure 7.9: The relative error of the total radial self-force, comparing two to three terms in the l-mode fit.

7.3.2 Fractional errors

I obtain the fractional error, within a given method for choosing the best self force, by dividing the standard deviation of the total self-force, over a range of l_{min} and l_{max} by the average. This is shown for median and fit methods in Figures 7.10 and 7.11, respectively. The two methods are clearly not consistent in detail of their evolution, though they give roughly the same order of magnitude averaged over time. The absolute error is the standard deviation itself. The absolute error, as a function of time, compared to the self-force itself, is shown in Figure 7.12. The two peaks do not obviously match periastron, apastron, or any specific phase of the orbit. *There is further work to be done here, specifically, I would like to redo this with the asymptote method.*

Relative error compares one model to a different model. Fractional error compares the spread of parameters within a model. The order of magnitude larger fractional error in the l-mode start and end points than in the relative error measurement of these start and end points points to the importance of the corrections in the surface in Figure 7.6. To obtain an estimate of the error that is better than a two order of magnitude range from 10^{-3} to 10^{-4}, it is necessary to perform either a proper second order Richardson extrapolation or a proper statistical study using covariances, hypothesis testing, and an as yet undiscovered method of handling biased estimators

60
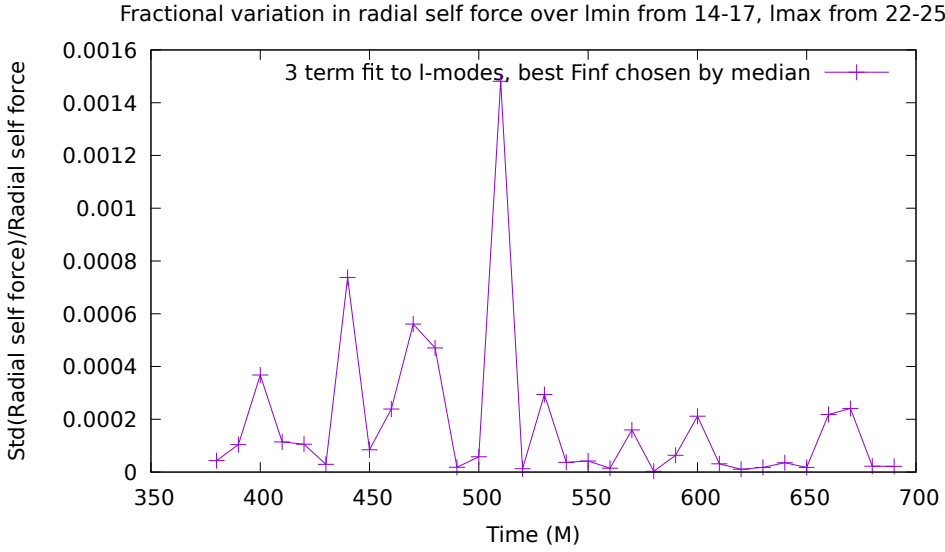
Figure 7.10: Fractional error in total radial self force, with average and standard deviation calculated over the surface shown in Figure 7.6. Fractional error is defined as standard deviation divided by average. This figure is for 3 terms in the fit, using the median method. Fractional error is at the level of 10^{-3}. F_{inf} was determined using the median method to determine F_{inf}.
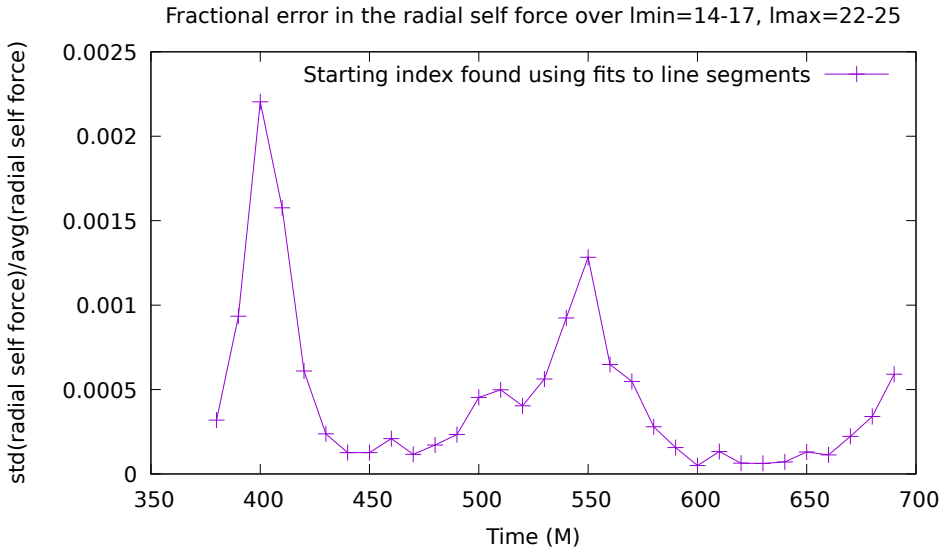
Figure 7.11: Fractional error in the total radial self force, with average and standard deviation calculated over the surface shown in Figure 7.6. Fractional error is defined as standard deviation divided by average. This figure is for 3 terms in the fit, using the fit method to determine F_{inf}. Fractional error is at the level of 10^{-3}. F_{inf} was determined using the fit method.
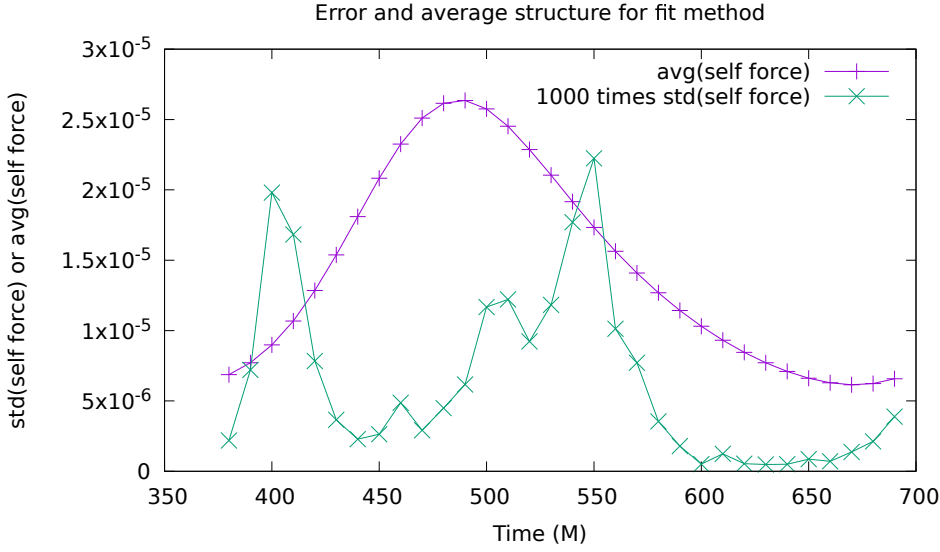
Figure 7.12: The structure of the standard deviation of Figure 7.6 in comparison to the evolution in time. This is for the fit method for determining F_{inf}.

and unmodelled noise.

7.4 Best choice l_{mins} and l_{max}'s and best choice DG orders

l_{min} can be as low as 14 and as high as 17, and l_{max} can be as low as 22 and as high as 25 without encountering roundoff or truncation error. The errors are dominated by correlations in the choice of the start and end modes. Relative error and fractional error, in the sense of a standard deviation divided by an average, appear to measure different things when correlated measurements are involved. If we take relative error as the quantity of interest due to standards of the numerical relativity field, the dominant error is at the 10^{-4} level. The primary effects are the selection of the number of terms in the mode-sum and the selection of start and end modes to achieve the regime in which the fit is valid and to eliminate roundoff noise. These results are very preliminary and further investigation is intended. *In particular, I will need to reproduce some of these plots and re-evalute the conclusions using the asymptote method or a further developed version of the fit method.* We hope they will improve.

Chapter 8
Future work: generic orbits via the osculating orbits framework

8.1   Plans for the more distant future

First, I will continue to work toward a solution to the peak in the relative difference between F_{inf} and the best DG order, 36, in Figure 6.11 using the asymptote method for determining F_{inf}. I will also need to re-evaluate most of the conclusions of Chapter 7.4 and possibly reassess best start and stop modes for the fit. Then I will update our comparison study using Niels Warburton's geodesic code for low l-modes to higher l-modes and use more recent versions of both codes. I will report the results to Niels Warburton and Peter Diener.

I also plan to run Peter Diener's simulation of scalar self-force on a Schwarzschild background for generic orbits including a back-reaction which causes the orbit to evolve away from a geodesic.

This is distinct from Warburton's code, in which the self force is generated in the frequency domain. It is assumed that the particle has been on the same orbit for all time, an assumption made necessary due to periodicity requirements. The evolution then happens in the time domain from one tangent geodesic to the next. This approximation is valid when the timescale of the orbital parameter change is much greater than the period of an orbit. Warburton's self-force does not include the evolving orbit and hence does not produce correct tails.

By contrast, in the time domain, in the self-consistent evolution the state of the field itself naturally accounts for the past history of the particle. In self-consistent evolution, the self-force takes into account the back-reaction that causes the particle to accelerate away from a geodesic. This requires accounting for two additional effects, that have already been implemented: the mass evolution and the acceleration term in the self-force.

Either the frequency or time domain initial data may be evolved in the time domain using two methods, the osculating orbits approach or the direct integration of the geodesic equation.

The osculating orbits approach should have more accuracy due to the monotonic evolution of χ and ϕ and the slow evolution of p and e, as opposed to the oscillating evolution of r and the four-velocity in the integration of the geodesic equation. I will run Peter Diener's simulation using Niels Warburton's frequency domain initial conditions with Barry Wardell's effective source and the osculating orbits evolution to analyze the physics of the self-consistent evolution.

Peter Diener, Ian Vega, Barry Wardell, and Steven Detweiler [11] have previously published on self-consistent evolution of a particle around a Schwarzschild black-hole; however, it did not have sufficient accuracy. We are attempting to improve the accuracy using entirely different numerical methods.

8.2 Self-consistent evolution

The long term goal of the field is self-consistent evolution. For a particle on a self-consistent orbit, it is necessary to include several additional effects. In addition to the wave equation with a source, the orbit evolves according to the geodesic equation, with the right hand side equal to the acceleration. The particle also gains or loses mass equal to the work being done on it.

$$
\begin{aligned}
\Box \Psi^R &= S_{eff} \\
ma^\alpha &= q(g^{\alpha\beta} + u^\alpha u^\beta)\partial_\beta \Psi^R \\
\frac{\partial m}{\partial \tau} &= -qu^\alpha \partial_\alpha \Psi^R_\alpha
\end{aligned}
\tag{8.1}
$$

The second equation gives the back-reaction due to acceleration of the particle. Here, Ψ^R is the regularized field. The third equation governs the self-consistent evolution of the mass of the particle. [59]

There are two methods for evolving the orbit that we may use, already implemented in the code by Peter Diener: direct integration of the geodesic equation and osculating orbits [46].

8.2.1 Direct integration of the geodesic equation

The geodesic equation is modified to include a force term on the right hand side in the presence of a self-force or external force [7].

$$\frac{d^2x^\mu}{d\tau^2} + \Gamma^\mu_{\rho\sigma}\frac{dx^\rho}{d\tau}\frac{dx^\sigma}{d\tau} = a^\mu \tag{8.2}$$

This equation, together with Equations 8.1, provide the basis for the generic evolution code when direct integration of the geodesic evolution is used.

8.2.2 Osculating orbits

An alternative approach is possible, based upon Reference [46]. In a Schwarzschild space-time, if the effect of the small black hole is neglected, there is a Killing vector along the time direction and in any angular direction, resulting in energy conservation and angular momentum conservation respectively. It is natural to evolve in a physical process that is closely related to these quantities. The eccentric orbit geodesic parameters p and e (semilatus rectum and eccentricity) are chosen (see Chapter 5.4). In either the geodesic approach or the self-consistent approach, the particle is accelerated, though in the self-consistent approach, that acceleration takes into account the particle's entire past history. In this process, p and e are updated at each time-step via a series of ordinary differential equations with extraordinarily complicated right hand sides. This is done using the same RK4 routine that is used to solve the wave equation. It will hopefully be more accurate than the geodesic evolution scheme because angular parameters ϕ and χ monotonically and smoothly increase while p and e evolve slowly, reducing truncation error. This is in contrast to the accumulation of error introduced through oscillations in r and the four-velocity in the geodesic method. In the self-consistent approach, mass will also ultimately be evolved.

8.3   Time line

I believe it will take me roughly one to four months to complete the re-evaluation of the methods in Chapter 7.4. It may take substantially longer if it is necessary to obtain large amounts of data to examine the second order Richardson extrapolation or if it is necessary to use formal

statistics for biased, correlated errors with hypothesis testing.

I expect that extracting physics from, and helping to address stabilities, debug, and possibly write code for prior to running, the Warburton/Diener simulations to obtain a comparison between the geodesic and osculating orbits approaches with the frequency domain initial data will take one to two years. Writing it into a paper and getting it published will take another year.

That totals about two to three years, when some leeway is allowed for writing the thesis.

References

[1] Amaro-Seoane, Pau; Gair, Jonathon R.; Pound, Adam; Hughes, Scott A.; Sopuerta, Carlos F. (2014). Research Update on Extreme-Mass-Ratio Inspirals. *arXiv:1410.0958v1*.

[2] Babak, Stanislav. (2017). Science with the space-based interferometer LISA. V: Extreme mass-ratio inspirals. *arXiv:1703.09722v1*.

[3] Bambi, Cosimo. (2017) Testing black hole candidates with electromagnetic radiation. *Reviews of Modern Physics* 89.

[4] Barack, Leor; Goldourn; Darren A. (2007). Scalar-field perturbations from a particle orbiting a black hole using numerical evolutions in 2+1 dimensions. *Phys. Rev. D* 76, 044020.

[5] Bernuzzi, Sebastiano; Nagar, Alessandro; Zenginoglu, Anil. (2011). Binary black hole coalescence in the large-mass-ratio limit: the hyperboloidal layer method and waveforms at null infinity. *arXiv:1107.5402v2*.

[6] Berti, Emanuele; Cardoso, Vitor; Starinets, Andrei O. Quasinormal modes of black holes and black branes. *arXiv:0905.2975v2*

[7] Carroll, Sean M. (2004). *An Introduction ot General Relativity Spacetime and Geometry.* Addison Wesley.

[8] Detweiler, Steven; Whiting, Bernard F. (2002). Self-force via a Green's function decomposition. *Phys. Rev. D* 67, 024025.

[9] Danzmann, Karsten. (2017). LISA Laser Interferometer Space Antenna: A proposal in response to the ESA call for L3 mission concepts.

[10] Damour, Thibault. (2015). 1974: the discovery of the first binary pulsar. *arXiv:1411.3930v2*.

[11] Diener, Peter; Vega, Ian; Wardell, Barry; Detweiler, Steven. Self-consistent orbital evolution of a particle around a Schwarzschild black hole. *arXiv:1112.4821v3*.

[12] Dirac, P. A. M. (1938). Classical theory of radiating electrons. *Royal Society Publishing.*

[13] Diaz-Rivera, Luz Maria; Messaritaki, Eirini; Whiting, Bernard F.; Detweiler, Steven. (2004). Scalar field self-force effects on orbits about a Schwarzschild black hole. *arXiv:gr-qc/0410011v1*.

[14] Field, Scott E.; Hesthaven, Jan S.; Lau, Stephen R. Discontinuous Galerkin method for computing gravitational waveforms from extreme mass ratio binaries. *arXiv:0902.1287v2*.

[15] Gillessen, S. ; Eisenhauer, F.; Fritz, T. K.; Bartko, H.; Dodds-Eden, K.; Pfuhl, O.; Genzel, R. (2009). The orbit of the star S2 around SGR A^* from VLT and Keck data. *arXiv:0910.3069v1*.

[16] Gair, Jonathan R.; Porter, Edward K. (2012). Observing extreme-mass-ratio inspirals with eLISA/NGO. *arXiv:1210.8066v1*

[17] Gralla, Samuel E.; Harte, Abraham I.; Wald, Robert M. (2009). A Rigorous Derivation of Electromagnetic Self-force. *arXiv:0905.2391v2*.

[18] Guzzetti, M.C.; Bartolo, N.; Liguori, M.; Martarrese, S. (2016). Gravitational waves from inflation. *arXiv:1605.01615v3*.

[19] Heffernan, Anna. (2012). The Self-Force Problem: Local Behavior of the Detweiler-Witing Singular Field. University College Dublin. *arXiv:1403.6177v1*.

[20] Heffernan, Anna; Ottewil, Adrian; Wardell, Barry; (2013). High-order expansions of the Detweiler-Whiting singular field in Schwarzschild spacetime. *arXiv:1204.0794v4*.

[21] Hesthaven, Jan S.; Warburton, Tim. (2008). *Nodal Disconintuous Galerkin Methods: Algroithms, Analysis, and Applications.* Springer.

[22] Hobbs, George; Dai, Shi. (2017). A review of pulsar timing array gravitational wave research. *arXiv:1707.01615v1*

[23] LIGO Virgo Collaboration. (2016). Observation of Gravitational Waves from a Binary Black Hole Merger. *Phys. Rev. Lett.* 116, 061102.

[24] LIGO Virgo Collaboration. (2016). GW151226: Observation of Gravitational Waves from a 22-Solar-Mass Binary Black Hole Coalescence. *Phys. Rev. Lett* 116, 241103.

[25] LIGO Virgo Collaboration. (2017). GW120104: Observation of a 50-Solar-Mass Binary Black Hole Coalescence at Redshift 0.2. *Phys. Rev. Lett.* 118, 221101.

[26] LIGO Virgo Collaboration. (2016). Observing Gravitational-wave Transient GW150914 with Minimal Assumptions. *Phys. Rev. D* 93, 122004.

[27] LIGO Virgo Collaboration. (2016). GW150914: First Results from the Search for Binary Black Hole Coalescence with Advanced LIGO. *Phys. Rev. D* 93, 122003.

[28] LIGO Virgo Collaboration. (2016). The Rate of Binary Black Hole Mergers Inferred from Advanced LIGO Observations Surrounding GW150914. *Accepted Astrophys. J. Lett*

[29] LIGO Virgo Collaboration. (2016). Astrophysical Implications of the Binary Black-Hole Merger GW150914. *Astrophys. J. Lett* 818, L22.

[30] LIGO Virgo Collaboration. (2016). Tests of General Relativity with GW150914. *Phys. Rev. Lett.* 116, 221101.

[31] LIGO Virgo Collaboration. (2016). GW150914: Implications for the Stochastic Gravitational Wave Background from Binary Black Holes. *Phys. Rev. Lett.* 116, 131102.

[32] LIGO Virgo Collaboration. (2016). Calibration of the Advanced LIGO Detectors for the Discovery of the Binary Black-hole Merger GW150914. *Submitted to Phys. Rev. D*.

[33] LIGO Virgo Collaboration. (2016). Characterization of Transient Noise in Advanced LIGO Relevant to Gravitational Wave Signal GW150914. *Class. Quant. Grav.* 33, 134001.

[34] LIGO Virgo Collaboration and ANTARES and IceCube Collaborations. (2016). High-energy Neutrino Follow-up Search of Gravitational Wave Event GW150914 with ANTARES and IceCube. *Phys. Rev. D* 93 122010.

[35] LIGO Virgo Collaboration. (2016). GW150914: The Advanced LIGO Detectors in the Era of First Discoveries. *Phys. Rev. Lett.* 116, 131103.

[36] LIGO Virgo, ASKAP, BOOTES, Dark Energy Survey and Camera, GW-EM, Fermi GBM and LAT, GRAWITA, INTEGRAL, IPTF, InterPlanetary, J-GEM, La Silla-Quest, Liverpool Telescope, LOFAR, MASTER, MAXI, MWA, PAN-STARRS, PESSTO, PI of the Sky, SkyMapper, Swift, TAROT, Zadko, Algerian National Observatory, C2PU, TOROS, and VISTA Collaborations. (2016). Localization and Broadband Follow-up of the Gravitational-wave Transient GW150914. *Astrophys. J. Lett.* 826, L13.

[37] Martynov, D.V., et al. (2016). Sensitivity of the Advanced LIGO detectors at the beginning of gravitational wave astronomy. *Phys. Rev. D* 93, 112004.

[38] Miller, Jeremy; Wardell, Barry; Pound, Adam. (2016). Second-order perturbation theory: the problem of infinite mode coupling. *arXiv:1608.0783v1*.

[39] Mino, Yasushi; Sasaki, Misao; Tanaka, Takahiro. (1996). Gravitational Radiation Reaction to a Particle Motion. *arXiv:gr-qc/9606018v1*.

[40] Misner, Charles W.; Thorne, Kip S.; Wheeler, John Archibald. (1973). *Gravitation.* W. H. Freeeman and Company.

[41] Newman, Mark. (2013). *Computational Physics.* University of Michigan.

[42] Philipp, Dennis; Perlick, Volker. (2015). On analytic solutions of wave equations in regular coordinate systems on Schwarzschild background. *arXiv:1503.08101v1*

[43] Poisson, Eric; Pound, Adam; Vega, Ian. (2011). The motion of point particles in curved spacetime. *Living Reviews in Relativity*. 14, 7.

[44] Pound, Adam. (2012). Second-order gravitational self-force. *arXiv:1201.5089v2*.

[45] Pound, Adam. (2017). Nonlinear gravitational self-force: second-order equation of motion. *arXiv:1703.02836v1*.

[46] Pound, Adam; Poisson, Eric. (2008). Osculating orbits in Schwarzschild spacetime, with an application to extreme mass-ratio inspirals. *Phys. Rev. D* 77, 044013.

[47] Press, William H.; Teukolsky, Saul A.; Vetterling, William T.; Flannery, Brian P. (2002). *Numerical Recipes in C++: The Art of Scientific Computing.* The Press Syndicate of the University of Cambridge.

[48] Price, Richard H. (1972). Nonspherical Perturbations of Relativistic Gravitational Collapse. I Scalar and Gravitational Perturbations. *Phys. Rev. D* 5, 10.

[49] Quinn, Theodore, C. (2000). Axiomatic approach to radiation reaction of scalar point particles in curved spacetime. *arXiv:qr-qc/0005030v1*.

[50] Quinn, Theodore C.; Wald, Robert M. An Axiomatic approach to electromagnetic and gravitational radiation reaction of particles in curved spacetime. *arXiv:gr-qc/9610053v1*.

[51] Saulson, Peter R. (1994). *Fundamentals of Interferometric Gravitational Wave Detectors.* World Scientific Publishing Co.

[52] Vega, Ian; Diener, Peter; Tichy, Wolfgang; Detweiler, Steven. (2009). Self-force with (3+1) codes: a primer for numerical relativists. *arXiv:0908.2138v1*.

[53] Vega, Ian; Wardell, Barry; Diener, Peter. (2011). Effective source approach to self-force calculations. *arXiv:1101.2925v1*.

[54] Vega, Ian; Wardell, Barry; Diener, Peter; Cupp, Samuel; Haas, Roland. (2013). Scalar self-force for eccentric orbits around a Schwarzschild black hole. *arXiv:1307.3476v2*.

[55] Vega, Ian; Wardell, Barry; Diener, Peter; Cupp, Samuel; Hass, Roland. (2013). Scalar self-force for eccentric orbits around a Schwarzschild black hole. *arXiv:1307.3476v2*.

[56] Volonteri, Marta. (2010). Formation of Supermassive Black Holes. *arXiv:1003.4404v1*.

[57] Wald, Robert M. (1984). *General Relativity.* The University of Chicago.

[58] Warburton, Nield; Akacay, Sarp; Barack, Leor; Gair, Jonathan R.; Sago, Norichika. (2013). Evolution of inspiral orbits around a Schwarzschild black hole. *arXiv:1111.6908v3*.

[59] Wardell, Barry. (2015). Self-Force: Computational Strategies. *arXiv:1501.07322v3*.

[60] Wardell, Barry; Vega, Ian; Thornburg, Jonathan; Diener, Peter. (2012). Generic effective source for scalar self-force calculations. *arXiv:1112.6355v3*.

[61] Wolfram, Stephen. (2016). *An Elementary Introduction to the Wolfram Language.* Wolfram-Media, inc.

[62] Yang, Huan; Zimmerman, Aaron; Zenginoglu, Anil; Zhang, Fan; Berti, Emanuele; Chen, Yanbei. (2013). Quasinormal modes of nearly extremal Kerr spacetimes: spectrum bifurcation and power-law ringdown. *arXiv:1307.8086v1*.

[63] Yunes, Nicolas; Wofgang, Tichy; Owen, Benjamin J.; Briigmann, Bernd. (2006). Binary black hole initial data from matched asymptotic expansions. *arXiv:gr-qc/0503011v3*.

[64] Yusef-Zadeh, F.; Wardle, M.; Schödel, R.; Roberts, D. A.; Cotton, W.; Bushouse, H.; Arendt, R.; Royster, M. (2016). SGR A^* and its environtment: Low-mass star formation, the origin of X-ray gas, and collimated outflow. *Astro. Ph. Journal*, 819, 60.

[65] Zenginoglu, Anil; Khanna, Gaurav. (2011). Null infinity waveforms from extreme-mass-ratio inspirals in Kerr spacetime. *arXiv:1108.1816v2*.

Vita

My past research has been on gravitational lensing and cosmology, exoplanets, neutrino oscillations, theoretical particle physics, gravitational waves, gravity gradient noise, and fractional calculus. Most of my background is in simulation, whether statistical or theoretical. I think of myself as a computational physicist and a multi-messenger astronomer.

I have 27 publications or preprints thanks in part to my membership in the LIGO Scientific Collaboration from 2009 to 2011. I made significant contributions to five of these, four related to LIGO and one related to exoplanets. I have also had the opportunity to submit, unsuccessfully, an additional first author paper on the simulation of fractional order circuit devices with Gary Bohannan at Saint Cloud State University.

When interpreting the name on this document, please understand that I am female to male transgendered and that my legal name is Susan Elaine Dorsher but that I go by Steven James Dorsher.